NEURAL DRUG DELIVERY: NOVEL MICROFLUIDIC DELIVERY DEVICES AND STUDIES OF TRANSPORT PHENOMENA

A Dissertation

Presented to the Faculty of the Graduate School

of Cornell University

In Partial Fulfillment of the Requirements for the Degree of

Doctor of Philosophy

by

Conor Patrick Foley

January 2009

NEURAL DRUG DELIVERY: NOVEL MICROFLUIDIC DELIVERY DEVICES AND STUDIES OF TRANSPORT PHENOMENA

Conor Patrick Foley, Ph. D.

Cornell University 2009

There are many promising pharmacological treatments for neurological disorders whose efficacies are limited by difficulties in delivering therapeutics to disease afflicted tissue. The work in this dissertation addresses some of the issues associated with neural drug delivery through three main investigative routes: development of new and more effective delivery devices, comprehension of drug transport mechanisms, and improvement in pre-clinical testing models for new therapeutics. A major focus of this work is convection enhanced delivery (CED). In CED, drugs are infused directly into tissue through a needle or catheter, and therefore are able to penetrate deeper into tissue than diffusion mediated delivery. A novel implantable microfluidic device was fabricated and characterized for chronic convection enhanced delivery protocols. The device consists of a flexible parylene microfluidic channel that is supported during tissue insertions by a biodegradable poly(DL-lactide-*co*-glycolide) scaffold. The device was able to reproducibly inject fluid into neural tissue with final infusate distributions that closely approximate delivery from an ideal point source. Also, real-time studies of drug transport through tissue were carried out using 2-photon excited fluorescence microscopy to monitor the movement of fluorescent nanoparticles in the rat cortex during delivery via CED. We found that perivascular spaces can drastically affect the distribution of therapeutic constructs larger than approximately 50nm by providing a high permeability conduit for transport through neural tissue. Finally, a

new endovascular microcatheter was developed that allows for selective intra-arterial injections in the rat brain. The device consists of a 169μm outer-diameter polyimide tube that has laser machined fluid delivery side-ports in the distal tip. A 450μm diameter by 1mm long poly(dimethyl siloxane) cylinder is attached to the distal end of the catheter to block blood flow in the carotid artery, to simulate an ischemic stroke. This device shows great promise for testing intra-arterial delivery of novel therapeutics in rat models.

BIOGRAPHICAL SKETCH

Conor Foley was born on the north side of Dublin, Ireland in July 1980. Fortunately, he quickly saw the error of his ways and moved back across the river Liffey, where he spent the rest of his childhood. In 1984 he joined the University College Dublin Chemical Engineering Society. He attended De La Salle College, Churchtown for secondary school, and completed his studies in 1999. He studied chemical engineering at University College Dublin, Ireland, graduating with a 1st class honors Bachelor of Engineering degree in 2003. In August 2003 he entered Cornell University to pursue his PhD in chemical engineering.

To my parents, John and Una Foley.

ACKNOWLEDGMENTS

The work presented in this dissertation would not have been possible without the help and support of a great number of people. The mentorship I have received from my advisor, William Olbricht, during my time at Cornell has been critical to my development as a scientist. He allowed me to forge my own path through my research, yet never allowed me to get too lost. I'd also like to thank the other members of my committee for their help with my research.

Keith Neeves taught me almost everything I know about microfabrication and made the lab an entertaining, stimulating, and occasionally abusive place to be. Keith was also a great person to travel the world with, despite his complete lack of a functional sense of direction.

I'd like also to express my sincerest gratitude to Chris Schaffer, Nozomi Nishimura, and the rest of the Schaffer research group members for their help and patience. They never seemed to grow weary of how I would show up, take over their lab, and occasionally break things. I know it can't have been easy.

David Putnam and the members of the Putnam group were kind enough to let me sit in their office, and treated me as one of their own. I'd especially like to thank Peter Zawaneh for always providing something to laugh at when the going got tough.

Walter Zink at Weill-Cornell Medical School has been one of the best collaborators anyone could hope to work with. His unwavering enthusiasm kept our project moving forward when it seemed all hope was lost. Hopefully someday soon we'll be able to watch the real Big Red at Memorial Stadium together.

I'd like to thank all the friends I've made during my time in Ithaca. Cormac Byrne and the rest of the Irish Graduate Students' Association helped to make Cornell feel a little bit more like the homeland. Robert Kuczenski and Benjamin F. Nicholson

were the best roommates I could ever hope to have. I'll never forget the two years I spent in the 'double-dub'. Jeff Fox and Ashlee McCaskill were integral in the success of Hector Street Smoke-Out I and II, despite the torrential rain (I), and bitter cold (II). They also made sure that fall football Saturdays will be one of my fondest memories of Ithaca. Geoff Genesky was a willing golf partner. Jordan Atlas somehow never got mad at me for constantly distracting him. The members of my first year class are too numerous to mention, but together they made that first year of grad school almost bearable. Without the support of Tricia Echtenkamp, I would never have made it this far.

Finally, I'd like to thank my family for their unending encouragement and love.

Portions of this work were supported by the National Institutes of Health Grant NS-045236 and were carried out in part at the Cornell NanoScale Facility, a member of the National Nanotechnology Infrastructure Network, which is supported by the National Science Foundation (Grant ECS-0335765). Also, this work made use of STC shared experimental facilities supported by the National Science Foundation under Agreement No. ECS-9876771. Parts of this research were funded by a Cornell University Intramural Seed Grant (2006).

"Years ago my mother said to me, 'In this world, Elwood, you must be oh so smart or oh so pleasant.' For years I was smart. I recommend pleasant."

- Mary Chase, Elwood P. Dowd (Jimmy Stewart) in "Harvey", 1950

TABLE OF CONTENTS

LIST OF FIGURES

LIST OF TABLES

CHAPTER 1

INTRODUCTION

Many promising pharmacological treatments for neural diseases exist, but the efficacies of the therapies are often limited by the difficulty of delivering drugs to the central nervous system (CNS). A major obstacle in neural drug delivery is the blood brain barrier (BBB), which prevents large molecules from passing from the vascular system to the brain. Because of the BBB, achieving physiologically relevant doses of drugs in neural tissue with systemic delivery can require extremely high, sometimes toxic, doses. To overcome these difficulties new delivery methods which circumvent the BBB and deliver drugs directly to affected areas of the brain are being developed.

In one such technique, a polymer containing the drug is implanted in the brain. Over time, either the polymer degrades (if it is bioresorbable), or the drug leaches from the polymer matrix, thereby releasing the encapsulated drug in a controlled manner at the desired site. This technique has been used to deliver 1,3-bis(2-chloroethyl)-1-nitrosourea (BCNU) [1, 2], methotrexate [3], taxol [4], dexamethasone [5], NGF [6, 7], and other compounds of interest in CNS therapies [8]. Implantable drug-containing polymers can produce extremely high concentrations at the point of release, but because drug transport is mediated by diffusion, the concentration decays exponentially with distance away from the implant. When this is combined with the fact that agents delivered to the brain interstitium are subject to rapid elimination via permeation through the brain capillary wall or metabolism within brain tissue, the result is that drugs delivered in this manner rarely penetrate more than 1–3mm in the tissue [4, 6]. While this is sufficient for some treatments, many diseases require that the drugs penetrate farther into tissue.

To increase the drug penetration and improve the spatial distribution of agents delivered directly to the brain, researchers have employed convection enhanced delivery (CED) [9]. In this technique, a solution containing the drug is injected into the brain through a small needle or catheter (20–30 gauge, 300–900μm OD). Transport is then driven by pressure gradients rather than concentration gradients, and the drugs are able to penetrate farther into the tissue compared with diffusive delivery. Many compounds have been delivered in both animal and human experiments using CED. For example, the infusion of small molecules [9-11], proteins [12-14], growth factors [15, 16], and nucleotides [17] has been examined in animals, and chemotherapy drugs [18, 19], proteins [20-22], and viral vectors [23, 24] have been administered in clinical trials in human patients.

Although CED shows promise for treating disorders of the central nervous system, many technological and biological issues still remain. Notably, the use of large needles or catheters causes significant tissue damage upon insertion [25], and can increase the extent of backflow for a given infusion rate [26]. In addition the tip of the needle can become occluded with tissue. Compounding these issues, neural tissue is a highly inhomogeneous, poroelastic medium, and therefore predicting the fate of infused compounds is extremely difficult.

The work presented in this dissertation addresses some of the issues with CED in two ways: development of novel microfluidic delivery systems that might outperform traditional needles and catheters for CED protocols; and elucidating mechanisms of drug transport through tissue during CED infusions.

Chapter 2 of this dissertation describes the design, fabrication, and characterization of a novel flexible microfluidic device for chronic CED applications. Experimental evidence suggests that flexible infusion devices may outperform traditional rigid needles and catheters in chronic infusions by decreasing the

mechanical mismatch between the implant and the tissue. This mismatch can cause micro-tearing of tissue in the area of the device tip which results in undesirable infusate distributions. To enable the device to be inserted into tissue a microfabricated insertion scaffold was designed. The scaffold supports the parylene channel during insertions, and then biodegrades in the tissue to leave the implanted device. This implantable system was characterized through *in vitro* and *in vivo* experiments, and was repeatedly able to deliver fluid to neural tissue, with final infusate distributions that closely approximate ideal infusions from a point source.

Chapter 3 addresses a different issue associated with CED. Since CED will be best utilized to administer large therapeutics that do not readily cross the BBB, it is of vital importance to understand how these constructs move through neural tissue when delivered to reduce leakage of drug from diseased tissue into healthy areas of the brain. Infusions of liposomes, viral vectors, high molecular weight tracers, and nanoparticles to neural tissue were shown to localize in the perivascular spaces of blood vessels within the brain parenchyma. In this chapter, 2-photon excited fluorescence microscopy was used to monitor the distribution of fluorescent nanoparticles delivered to the cortex of rats via CED using microfluidic probes. This imaging technique permits studies on much finer temporal and spatial scales than can be achieved with other imaging modalities, such as MRI. The results of these studies show that for large particles which are hindered from easily passing through the extracellular matrix, perivascular spaces provide a high permeability path for transport through tissue. The transport of nanoparticles through perivascular spaces was size dependant. Larger nanoparticles (100nm nominal diameter) were not distributed throughout the tissue, and a higher fraction of the infused particles were restricted to the perivascular spaces and did not localize in the extracellular space. Similarly, perivascular spaces were the preferred path for smaller nanoparticles (24nm nominal

diameter), though these particles were not entirely excluded from the extracellular matrix and were able to pass through the bulk tissue when no perivascular spaces were present, even at relatively low flow rates.

Chapter 4 summarizes efforts to develop a microfluidic device for intra-arterial selective injection. In this technique a catheter is passed into the carotid artery where it can inject drugs into different branches of the intracranial arteries. This procedure has been most widely used in the field of interventional neuro-radiology as a way to treat ischemic stroke, i.e. the intra-arterial injection of recombinant tissue plasminogen activator. Intra-arterial selective injection could also be used to deliver drugs that might protect brain cells from undergoing apoptosis after reestablishing blood flow in cases of ischemic stroke – known as selective intra-arterial neuro-protection. This chapter describes the fabrication and characterization of a novel endovascular microfluidic catheter of use in small animal trials of candidate drugs for selective intra-arterial neuro-protection. The microcatheter must be able to reversibly simulate an ischemic stroke, and selectively inject different branches of the intracranial arteries of the rat. The catheter was made from 169μm outer-diameter polyimide tubing that had fluid delivery side-ports laser machined in the distal tip. To simulate the occlusion of the carotid artery a 450μm outer-diameter by 1mm long PDMS cylinder was attached to the distal tip of the catheter. This microcatheter was tested in rats, and successfully replicated a reversible stroke, and selectively injected different branches of the intracranial arteries.

Finally, chapter 5 summarizes the salient findings of the work in this dissertation, and provides discussion of what the future work on these problems might entail.

CHAPTER 2

FLEXIBLE MICROFLUIDIC DEVICES SUPPORTED BY BIODEGRADABLE INSERTION SCAFFOLDS FOR CONVECTION ENHANCED NEURAL DRUG DELIVERY

2.1 Introduction

Convection enhanced delivery (CED) is a promising new technique for treating neurological disorders. In CED drugs are infused directly into tissue through a needle or catheter [9]. This technique circumvents the blood brain barrier and can achieve high local concentrations of drug with fewer side effects than with systemic delivery. Because many agents delivered directly to the brain are subject to rapid elimination from the interstitial space via permeation through the capillaries or metabolism within brain tissue [27], drugs delivered by diffusion from polymer implants or bolus injections are often only able to penetrate a small distance (approximately 1-3mm [4, 6]) from the implant. Since drug transport in CED is driven by pressure gradients rather than diffusion along concentration gradients, drugs can penetrate to tissue that is much further from the delivery site. Many compounds have been delivered in both animal and human experiments using CED. For example, the infusion of small molecules [9-11], proteins [12-14], growth factors [15, 16], and nucleotides [17] has been examined in animals, and chemotherapy drugs [18, 19], proteins [20-22], and viral vectors [23, 24] have been administered in clinical trials in human patients.

However, current CED protocols that use standard needles and catheters are not suitable for chronic applications because of problems with tissue damage upon

insertion, backflow along the needle path, occlusion of the needle tip, and the tissue's foreign body response. Microfabricated devices can offer many advantages over standard needles. Primarily, their small size limits tissue damage [25] and backflow [26]. Also, it is possible to locate the fluidic outlet away from the leading edge of the device to reduce occlusion of the fluidic channel. Furthermore, with current microfabrication technology it is possible to create devices with features that are not available with standard needles, e.g. recording and stimulating electrodes, chemical and mechanical sensors that could allow the device to respond to changes in tissue physiology, and multi-channel fluidics for delivering different compounds in a controlled regimen.

Several researchers have created microfluidic silicon probes for use in the brain. Although these devices moderate backflow and the initial tissue damage due to insertion [28-30], they may not be particularly well suited for chronic implantation as the brittle nature of silicon increases the risk of a probe breaking inside the tissue. In addition, silicon probes have been found to cause a significant foreign body response [25, 31].

Researchers have shown that flexible catheters perform better than rigid catheters in chronic infusion studies in rats. Guarnieri *et al* [32] examined the effect of rigid and flexible catheters on the delivery of carboplatin and doxorubicin in both healthy and disease challenged rat brains, and found that the drug distributions delivered by the flexible catheters more closely approximated the theoretical ideal distribution from a point source than the distributions delivered by rigid catheters. They hypothesize that this difference is caused by micro-tearing in the area around the rigid catheters due to relative motion between the brain and the implant, which creates a high permeability path for fluid to escape the intended delivery area. Flexible catheters may be able move with the brain, thus eliminating micro-tearing and

maintaining the close contact between the device and the tissue required for controlled delivery. This suggests that in treatments that use CED for chronic applications, flexible catheters could outperform traditional rigid devices. The feasibility of long term CED protocols has already been examined in clinical trials. A phase I trial examining the effect of year long infusions of GDNF in Parkinson patients found that there were significant increases in dopamine storage in the putamen as a result of the treatment [33]. However, subsequent phase II trials failed to replicate the success of that study [34]. To determine why this trial failed, Salvatore and coworkers infused GDNF into the putamen of Rhesus monkeys for 7 days, and conlcuded that the trial had not been successful because the infusate localized around the tip of the catheter and did not distribute widely in the tissue [35]. This result may be due to microtearing of the tissue around the implanted device. The use of a more flexible infusion catheter may reduce these problems and improve the efficacy of the treatment.

Another neurological disease that may benefit from the application of chronic CED protocols is the highly aggressive brain tumor glioblastoma multiforme. This is an infiltrative tumor with cells that migrate away from the main tumor mass into healthy tissue [36]. In this case, CED is used to infuse into the tissue after the main tumor has been resected [37]. It is also used as a xenograft model to test the effectiveness of new drugs under development [38-40]. In both of these cases, it would be useful to be able to deliver drugs repeatedly, based on tumor growth, at exactly the same location. It is very difficult to reinsert a needle or catheter for repeated applications of a drug at precisely the same location in tissue for a variety of reasons, and even if this were achieved, each insertion leaves a needle track that affects subsequent infusions. A chronically implantable device such as the one presented here is well-suited for repeated CED therapy.

Although flexible polymer microfluidic devices may demonstrate better long-

term biocompatibility than silicon probes, their low rigidity makes them difficult to insert into tissue. To create chronic drug delivery implants that combine the desirable traits of small size and low rigidity, we constructed flexible parylene microfluidic devices supported by rigid scaffolds from poly(DL-lactide-*co*-glycolide) (PLGA, a biodegradable polyester). These scaffolds brace the flexible parylene device during insertion, but then degrade to leave the fluidic device in place in the tissue. Parylene was used for the microfluidic probe because it has many desirable characteristics. It has excellent dielectric properties (making it suitable for insulating electronics on the devices), it can be deposited using chemical vapor deposition (CVD) in uniform and consistent layers, and it is biologically compatible (meeting FDA class VI requirements). PLGA products are widely used in biomedical engineering applications as resorbable sutures [41], orthopedic implants [42], microspheres for controlled drug delivery [43], and tissue engineering scaffolds [44]. PLGA structures are generally formed in two ways, through solvent removal techniques [45] and through thermal embossing, where the polymer is heated above its glass transition temperature and formed into the appropriate shape [46, 47]. In this work the flexible microfluidic devices were constructed using top-down microfabrication techniques on a silicon wafer, and the degradable scaffolds were formed by hot-embossing the PLGA in a poly(dimethysiloxane) (PDMS) mold.

It has been found that PLGA structures display size-dependent degradation where larger structures undergo bulk degradation and smaller devices display only surface erosion [48]. As our scaffolds are close to the reported cut-off size, we examined the *in vitro* degradation time of the PLGA supports to determine how they degrade. We found that the scaffolds degrade with the manufacturers reported degradation time, which suggests that they undergo bulk degradation.

The performance of the microfluidic devices was examined through infusions

of dye into agarose gel brain phantoms and acute injections into the striatum of C57BL/6 mice. The devices were capable of both penetrating tissue and delivering fluid in a controlled and reproducible way.

2.2 Materials and Methods

2.2.1 Parylene Microfluidic Devices

The flexible parylene devices were produced on a silicon wafer using standard MEMS fabrication techniques. A schematic of the fabrication procedure is shown in Figure 2.1. A CF_4 plasma was used to roughen the surface of a clean 100mm single side polished silicon wafer before an 8μm thick layer of parylene-C was deposited using chemical vapor deposition (PDS 2010 LabCoter, Specialty Coating Systems, Indianapolis IN). This layer formed the base of the fluidic device. Next, photoresist (Shipley 1045) was spun on the wafer to a depth of 11μm (the intended height of the channels). This initial layer of photoresist was then patterned using contact lithography. The remaining photoresist defined the inside of the channels. A second 8μm thick film of parylene C was then deposited to form the top of the microfluidic device. Next, a 150nm thick aluminum etch mask was deposited via e-beam evaporation (Mark 50 E-beam evaporation system, CHA Industries, Fremont CA). This mask was then patterned with a second photolithography step, and the exposed aluminum was removed via a wet-etch. An oxygen RIE (PlasmaLab 80+ RIE system, Oxford Instruments, Oxfordshire, UK) was then used to etch through the parylene to the silicon wafer which defined the device body and opened the ends of the channels. Finally, the photoresist inside the channels was dissolved in acetone. The probes could then be easily peeled from the wafer to form free-standing parylene microfluidic

devices. A detailed fabrication description is presented in Appendix I.

2.2.2 Biodegradable Insertion Scaffolds

The PLGA insertion scaffolds were formed by hot-embossing PLGA granules in a poly(dimethylsiloxane) (PDMS) mold. To make the master mold, a silicon wafer was patterned using photolithography and selectively etched using a Bosch DRIE process (Unaxis SLR 770) to a depth of 200μm. This wafer was then silanized with tridecaflouro – 1,2,2 tetrahydrooctyl trichlorosilane before the PDMS mold was cast to prevent the mold from bonding to the master. To cast the PDMS mold, PDMS base and curing agent (Sylgard 184 silicone elastomer kit, Dow Corning, Midland MI) were mixed in a 10:1 weight ratio, and the mixture was thoroughly degassed. The mixture was then poured over the silicon master and cured at 70°C for three hours. When the mold had cured, it could be peeled from the master and used for hot-embossing.
The scaffolds were formed using a method similar to that demonstrated by Yang *et al* [47]. A schematic of the hot embossing procedure is shown in Figure 2.2. Granules of PLGA (5050 DL 3.5A, Lakeshore Biomaterials, Birmingham AL) were placed on the mold and a second piece of non-patterned PDMS was placed on top. This sandwich was placed in a laboratory press with heated platens, heated to 150 – 160°C and pressed at approximately 3.5MPa for 5 – 10min. The assembly was cooled to below the glass transition temperature of the PLGA by circulating water through the platens. The sandwich was then disassembled, and the finished PLGA scaffolds could be cleanly removed from the mold.

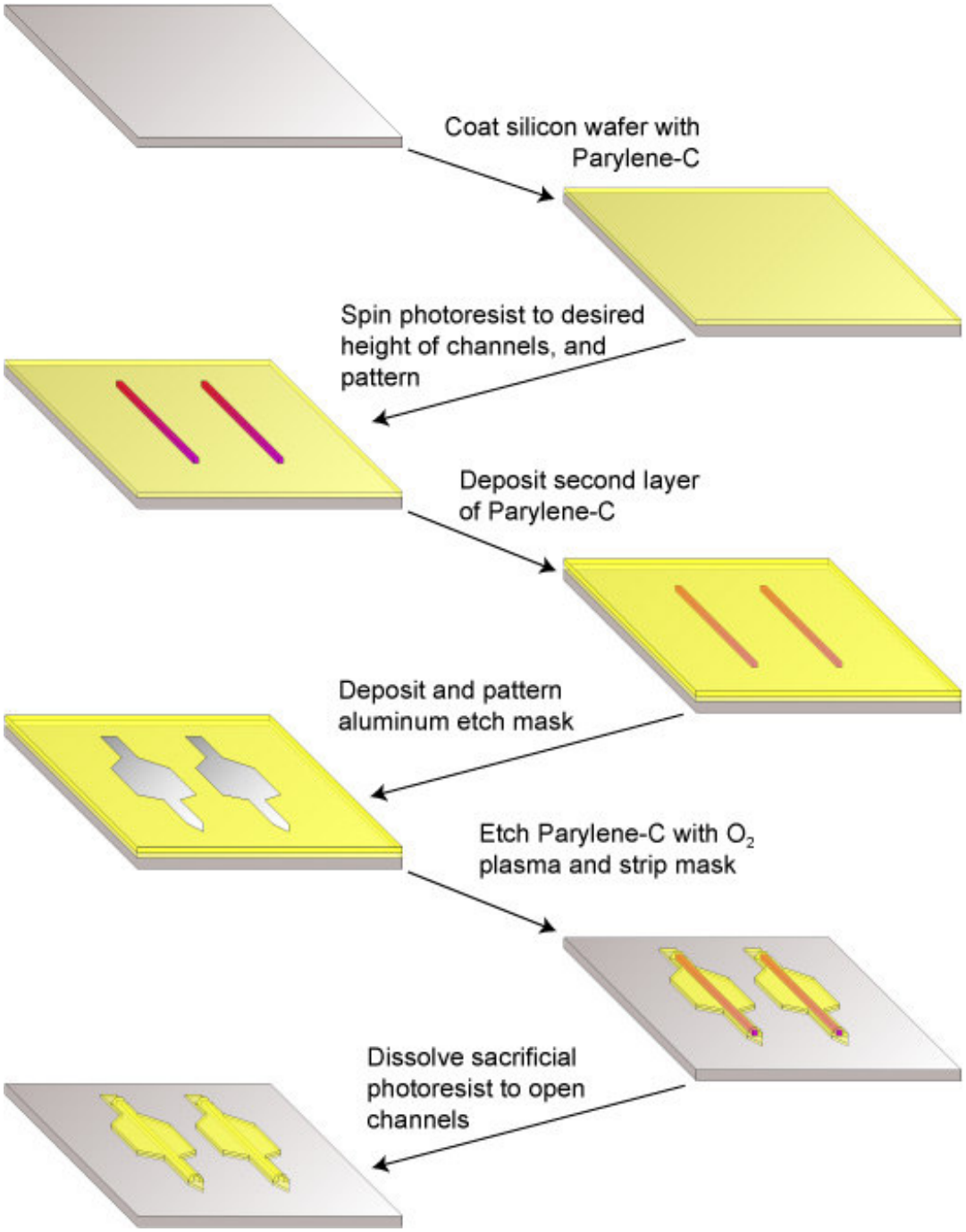

Figure 2.1. Fabrication schematic for flexible parylene microfluidic devices.

2.2.3 Device Assembly and *In Vitro* characterization

To connect the microfluidic device to external tubing, one of the probe shanks was inserted into a 7cm length of PEEK tubing (150µm ID, 360µm OD) (Upchurch Scientific, Oak Harbor WA) and sealed in place using a two-part epoxy (Epoxy 907, Miller-Stephenson, Danbury CT). The other end of the PEEK tubing was glued into the end of a borosilicate micropipette (1mm OD, 0.58mm ID) (World Precision Instruments Inc., Sarasota FL) using more epoxy. The parylene probe and PEEK tubing were fully primed with the fluid to be infused under vacuum, and then the micropipette was backfilled using a syringe with a 28 gauge MicroFil needle tip (World Precision Instruments Inc.). The micropipette served as the fluidic reservoir for the parylene device. The proximal end of the glass micropipette was connected to a programmable pressure injector (PM8000, World Precision Instruments Inc.) using a micro-electrode holder. To infuse fluid using the parylene device a constant pressure was applied to the fluidic reservoir in the micropipette via the pressure injector. The volumetric flow rate was determined by measuring the speed of the meniscus in the lumen of the micropipette.

To attach the microfluidic device to the insertion scaffold a small drop (~15µl) of 5-min epoxy (Devcon, Danvers MA) was placed on the body of the scaffold and the primed microfluidic device was carefully laid on top under a stereoscope. The cured epoxy coupled the body of the scaffold to the body of the parylene device, leaving the shanks aligned but not connected. The shanks were then sealed together by briefly dipping them in dichloromethane. This treatment removes the highly permeable fluidic track between the two parts of the system. The device assembly was allowed to air dry for at least 15 min to ensure that all residual dichloromethane had evaporated.

To allow the device to be inserted smoothly and reproducibly, the body of the

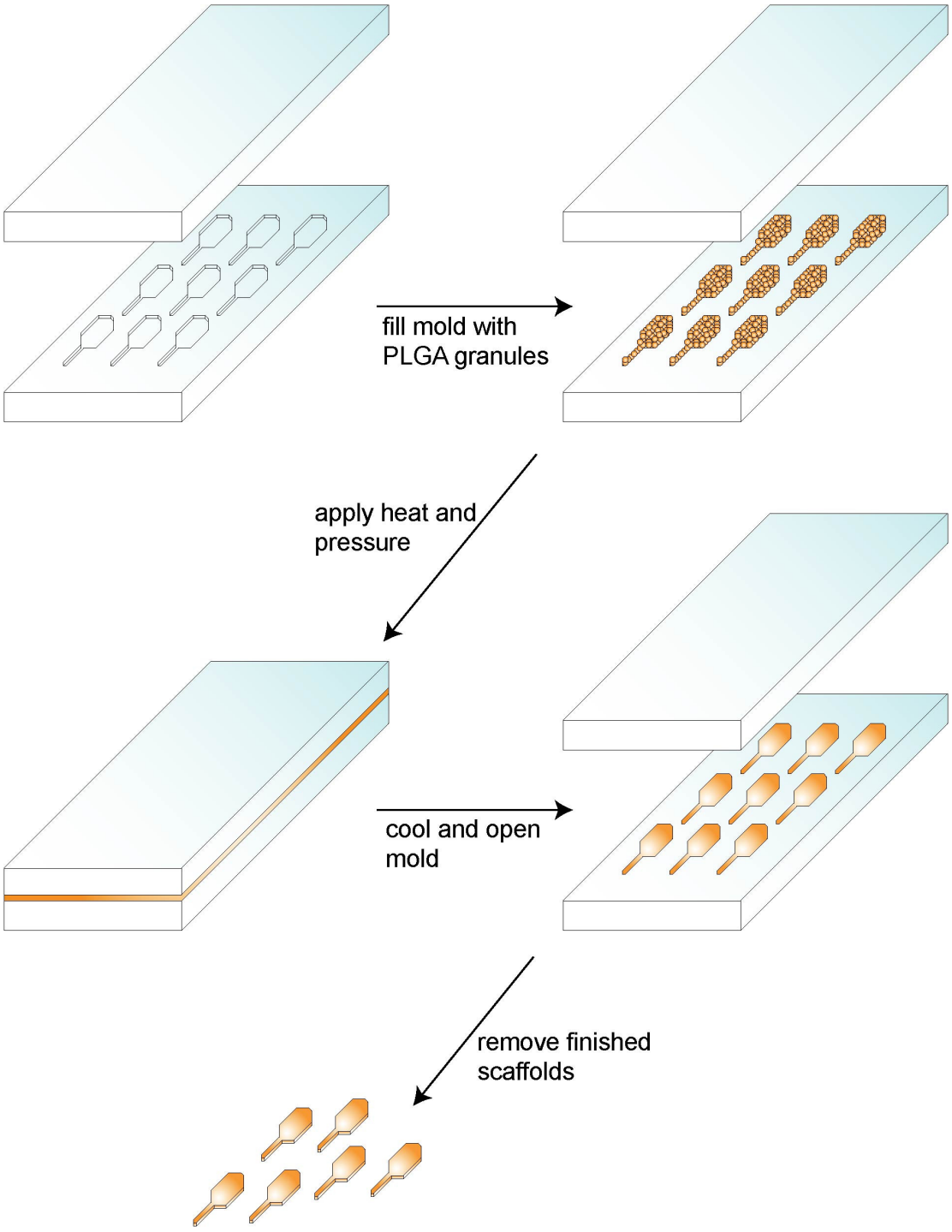

Figure 2.2. Fabrication schematic for hot embossing of PLGA insertion scaffolds.

scaffold/probe assembly was attached via double-sided adhesive tape to a custom made Delran block which was mounted on a micromanipulator.

This scaffold/microfluidic assembly was tested in a 0.6wt % agarose gel brain phantom to verify that the scaffolds were capable of penetrating tissue and that the microfluidic channels remained patent. To examine the effect of dichloromethane treatment on the performance of the channels, the flow rates obtained for a range of driving pressures (6.9, 17.2, 34.5, 68.9, and 103.4 kPa) were compared before and after dichloromethane treatment.

2.2.4 PLGA Scaffold Degradation Studies

In vitro degradation studies were carried out to determine the degradation time of the insertion scaffolds. PLGA scaffolds were weighed and placed in 50mM HEPES buffer containing 10mM KCl and 0.1% wt/v NaN3 (pH 7.4) and incubated at 37°C. Samples were removed every third day, washed, lyophilized and examined for gravimetric weight loss and molecular weight loss using GPC. The pH of the buffer was monitored and replaced with fresh buffer if the acidic degradation products caused the pH to drop below 7.3.

2.2.5 Acute *In Vivo* Infusions

Five male C57BL/6 mice weighing between 22 and 25g were anesthetized by an intraperitoneal injection of ketamine/xylazine (0.1mg/10g mouse ketamine, 0.1mg/10g mouse xylazine). Animals were then secured in a stereotactic frame, and an incision was made in the skin along the dorsal midline of the skull. A small craniotomy (3mm diameter) was made over the left side of the exposed skull using a dental drill. The

probe and attached scaffold were implanted using a micromanipulator 0.5mm anterior, 2.5mm medioateral, and 3mm deep from bregma. The device was then left implanted for 2 min to allow the tissue to equilibrate before starting the infusion. Evan's Blue dye (2wt% in phosphate buffered saline) was infused using a starting infusion pressure of 0.69kPa, and the infusion pressure was increased at a rate of 0.69kPa/30s to the final infusion pressure of 3.45kPa. After 1µl of dye had been injected, the infusion was stopped. The probe was left in the tissue for 2 min before being removed. The animal was removed from the stereotactic frame and immediately sacrificed via cardiac injection of urethane. The brain was then promptly extracted and frozen on dry ice. The frozen brain was sectioned into 20µm thick slices on a cryostat and every third slice was retained for imaging. All procedures were carried out in accordance with the Cornell University Institutional Animal Care and Use Committee guidelines and regulations.

2.2.6 Image Analysis

Tissue slices were imaged using a stereoscope and CCD camera. The captured RGB TIFF files were analyzed using ImageJ software (NIH, Bethesda MD) and a custom macro. The macro adjusted the contrast of the image, and split the RGB image into its constituent colors. The macro then took the red image, adjusted the contrast and converted the image to binary where the area stained with Evan’s Blue dye was white, and the rest of the image was black. Next, noise was removed from the image by replacing each pixel with the median value in its 3×3 neighborhood. Finally, the area of the white pixels was summed to get the area of the Evan’s Blue spot. The volume of distribution of the dye was calculated by summing the areas of distribution in each slice and multiplying the total by three times the slice thickness (to account for

discarded sections).

2.3 Results

2.3.1 Parylene Probes and Insertion Scaffolds

The parylene microfluidic devices had an overall length of 10.3mm and a 2mm wide body for ease of handling. The insertable shank was 150µm wide and 3.225mm long (Figure 2.3). The devices were very flexible, and not rigid enough to penetrate tissue unaided (Figure 2.4). The microfluidic fluidic channel was 11.4µm high, 50µm wide, and had two openings at the inlet and outlet of the device to minimize occlusion (Figure 2.5).

The hot embossing technique was capable of rapidly producing highly uniform insertion scaffolds. The scaffolds were measured under an optical microscope and were slightly larger (< 10%) than the original silicon master, most likely because of thermal expansion of the PDMS mold during the embossing process. Scanning electron micrographs of the scaffold shank and tip are shown in Figure 2.6.

2.3.2 *In Vitro* Performance

The fluidic devices were easily inserted into agarose gel phantoms. Also, the dichloromethane treatment used to seal the shanks of the scaffold and parylene device together had no effect on the flow characteristics of the device. We were able to infuse dye solutions into the brain phantoms with negligible backflow, and the observed distributions closely approximated the spherical distribution of an ideal point source.

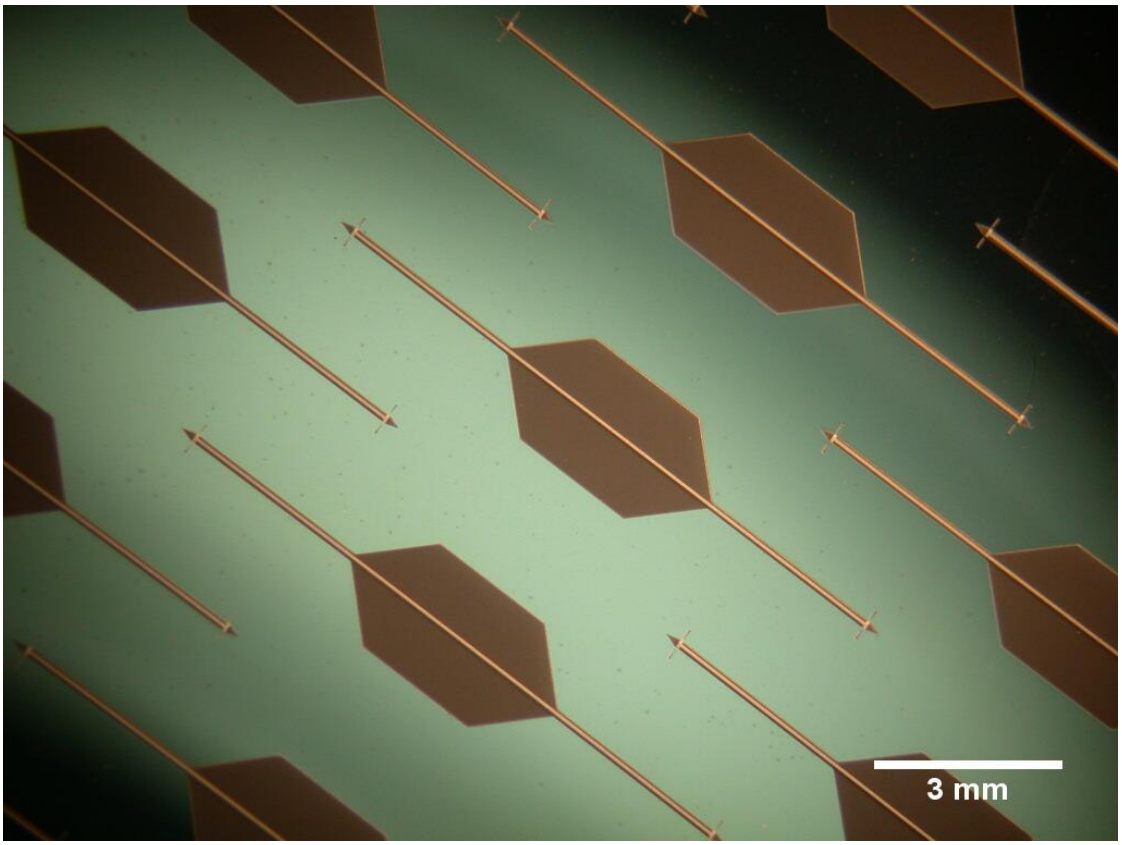

Figure 2.3. Whitelight image showing finished parylene microfluidic devices before they are removed from the silicon wafer.

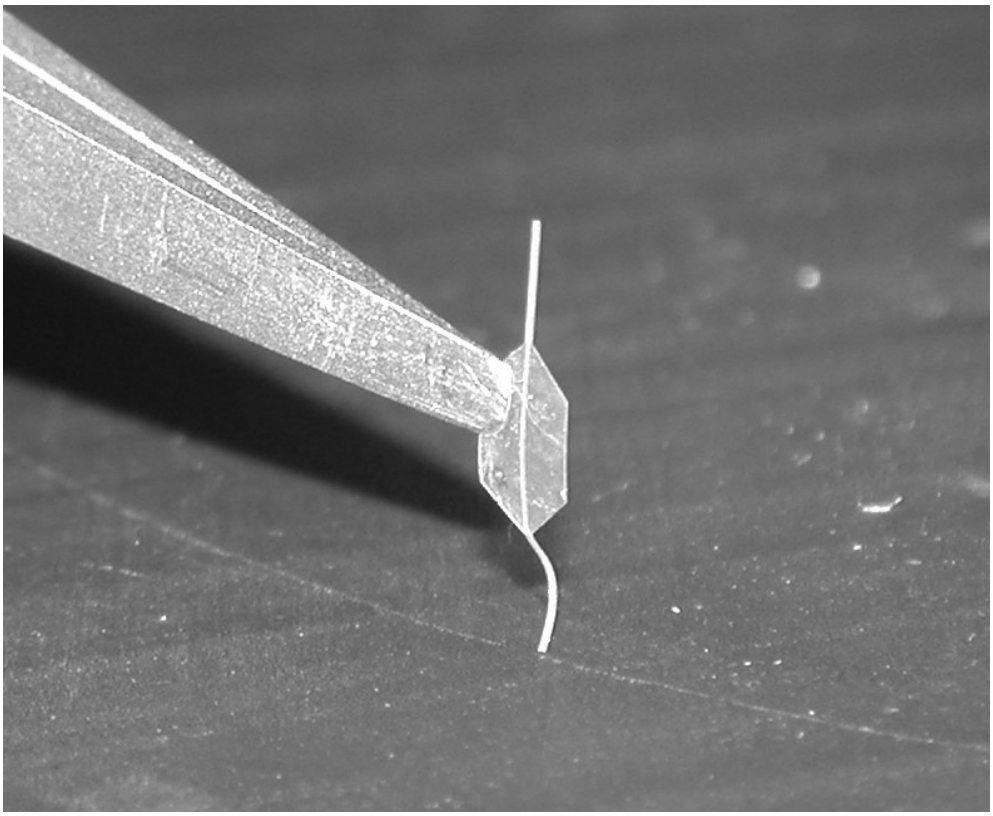

Figure 2.4. Photograph demonstrating the flexibility of the parylene devices.

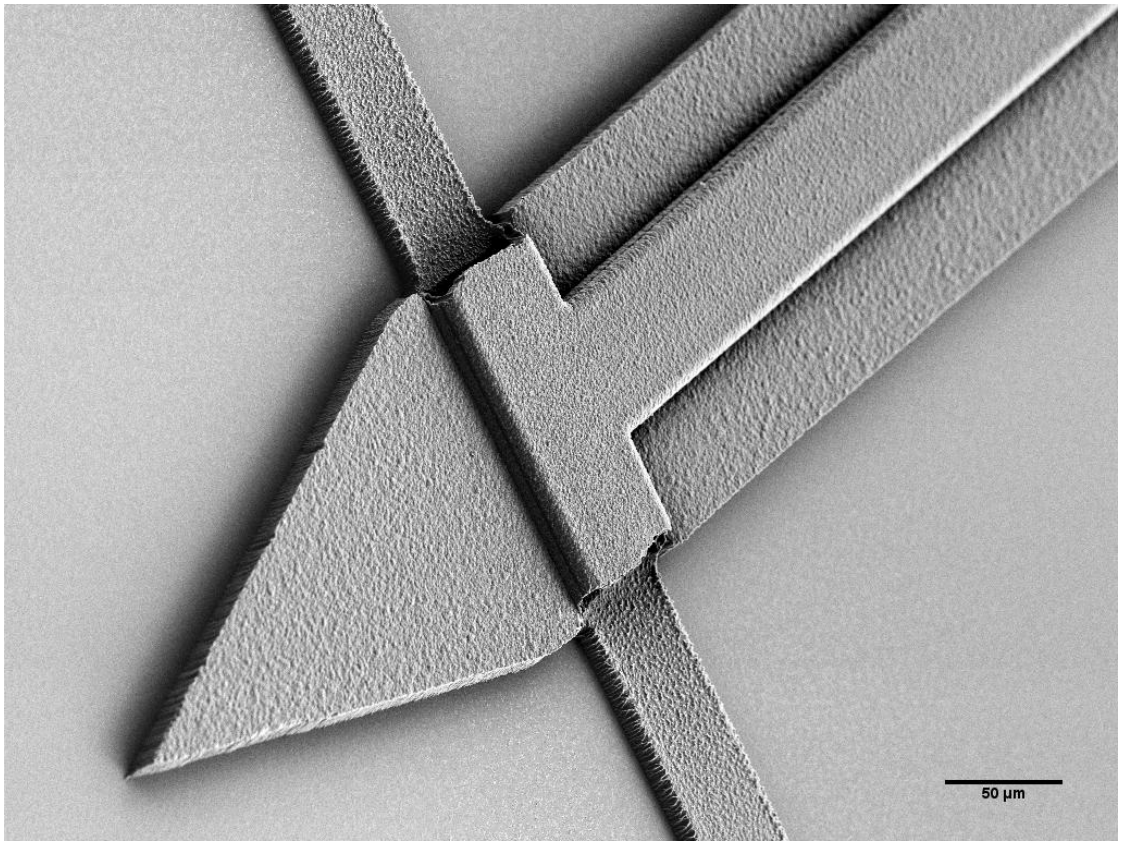

Figure 2.5. Scanning electron micrograph of the tip of the flexible parylene device. Note the two channel openings.

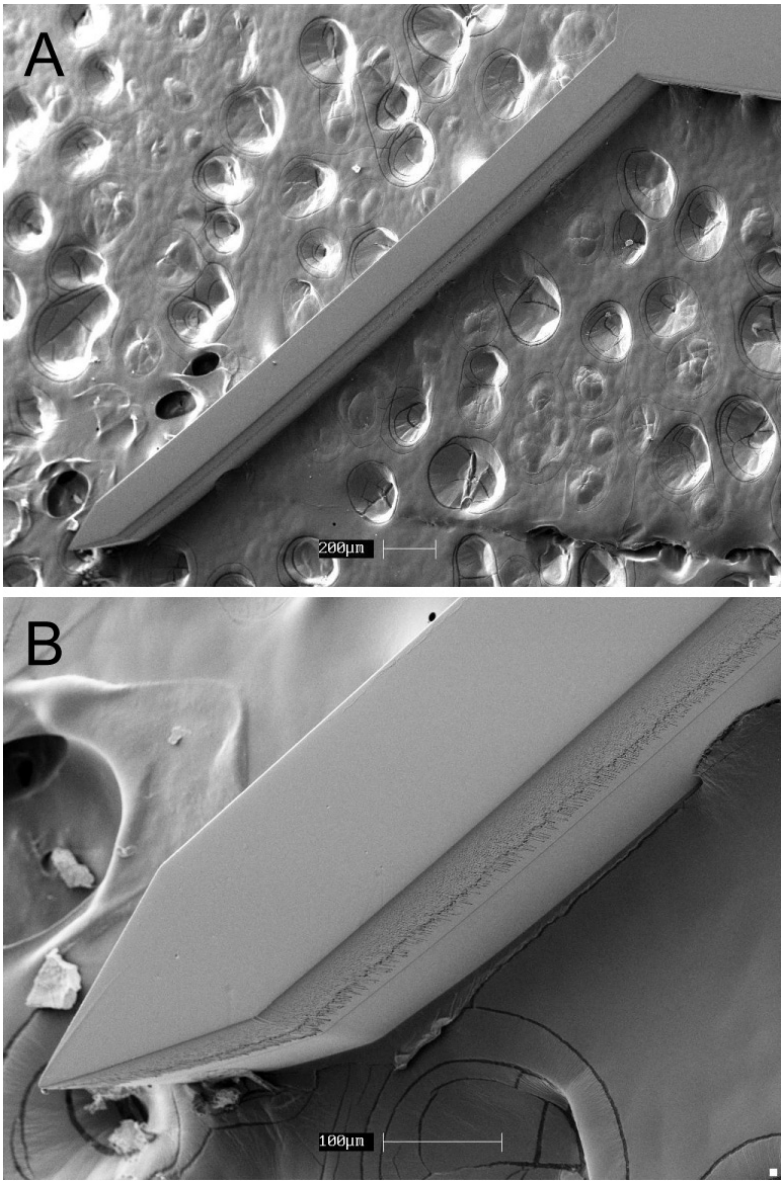

Figure 2.6. Scanning electron micrographs showing the (A) insertable shank of the PLGA scaffold, and (B) the tip of the scaffold. Note the striations on the side of the device in (B). These are artifacts of the deep silicon etch used to define the master.

Figure 2.7 shows the results of an infusion of green food dye into a 0.6wt% agarose gel brain phantom at a flow rate of approximately 0.1µl/min.

2.3.3 PLGA Scaffold Degradation Study

The scaffolds used in the degradation study had an average initial weight of 2.37 ± 0.41mg. The gravimetric weight loss as a function of time in the degradation buffer is shown in Figure 2.8. Figure 2.9 shows the molecular weight loss as a function of time and represents the extent of hydrolysis in the polyester backbone of the scaffolds. The gravimetric weight loss is a representation of the rate that the oligomers formed by hydroloysis of the PLGA backbone escape from the bulk of the structure. The scaffolds were almost 100% degraded after 27 days, but were observed to be swollen and had no rigidity after only 15 – 18 days. This was comparable with the manufacturer's reported time (3 – 4 weeks), and indicates that these scaffolds are large enough to undergo bulk degradation rather than surface erosion.

2.3.4 *In Vivo* Performance

The parylene devices were used to infuse Evan's Blue dye into the striatum of mice. The system was able to easily penetrate the tissue, and was able to deliver fluid in a reproducible distribution. The average flow rate obtained in the *in vivo* experiments was 0.09 ± 0.005µl/min (n = 5), at a driving pressure of 3.45kPa.

The volume of distribution (V_d) of the infusate was 5.17 ± 0.36mm^3 (n = 5). Figure 2.10 shows an example of a brain section showing the distribution of Evan's Blue and the corresponding binary image that was used to determine V_d. Figure 2.11 shows a plot of the average area of the dye distribution in a section as a function of the

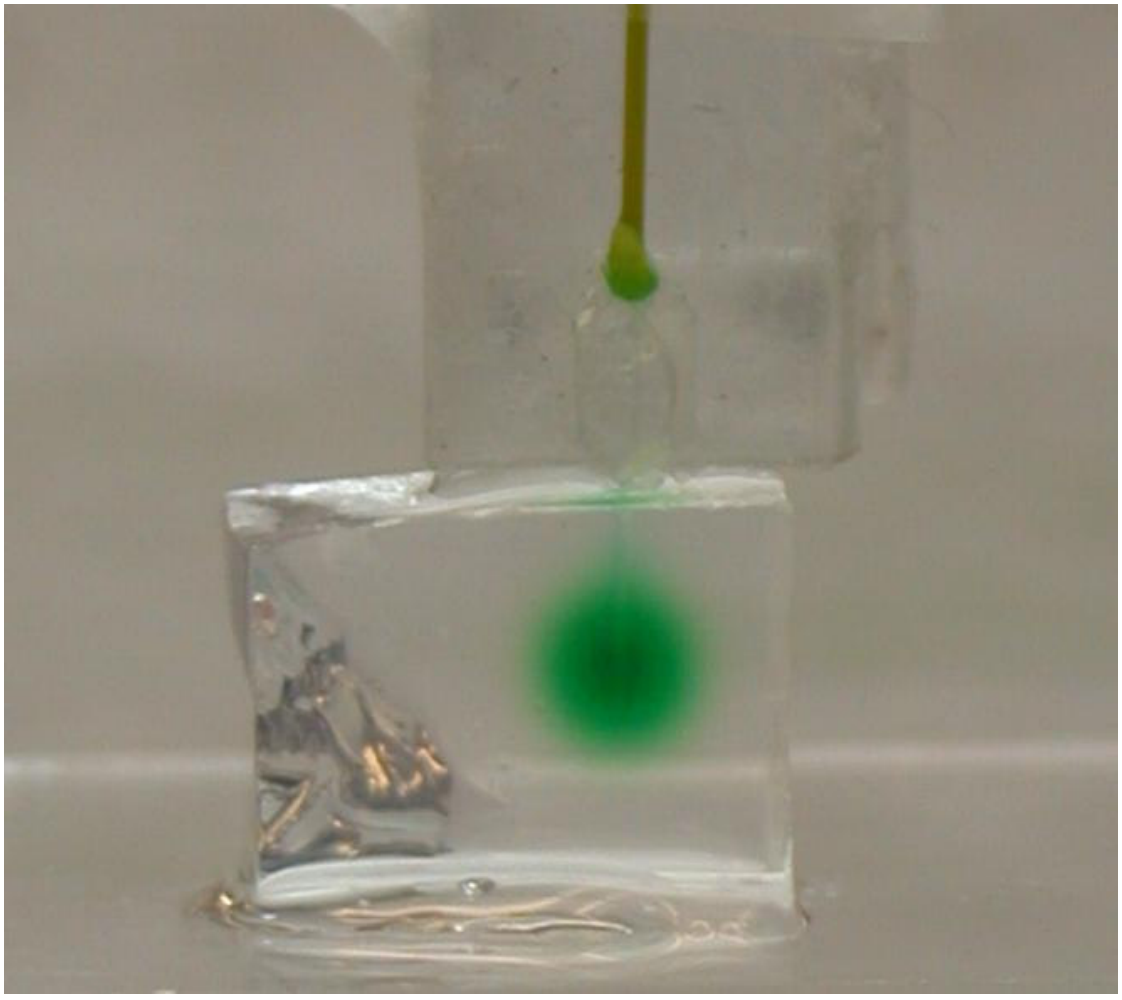

Figure 2.7. Photograph showing results of a test infusion of green food dye into a 0.6wt% agarose gel brain phantom.

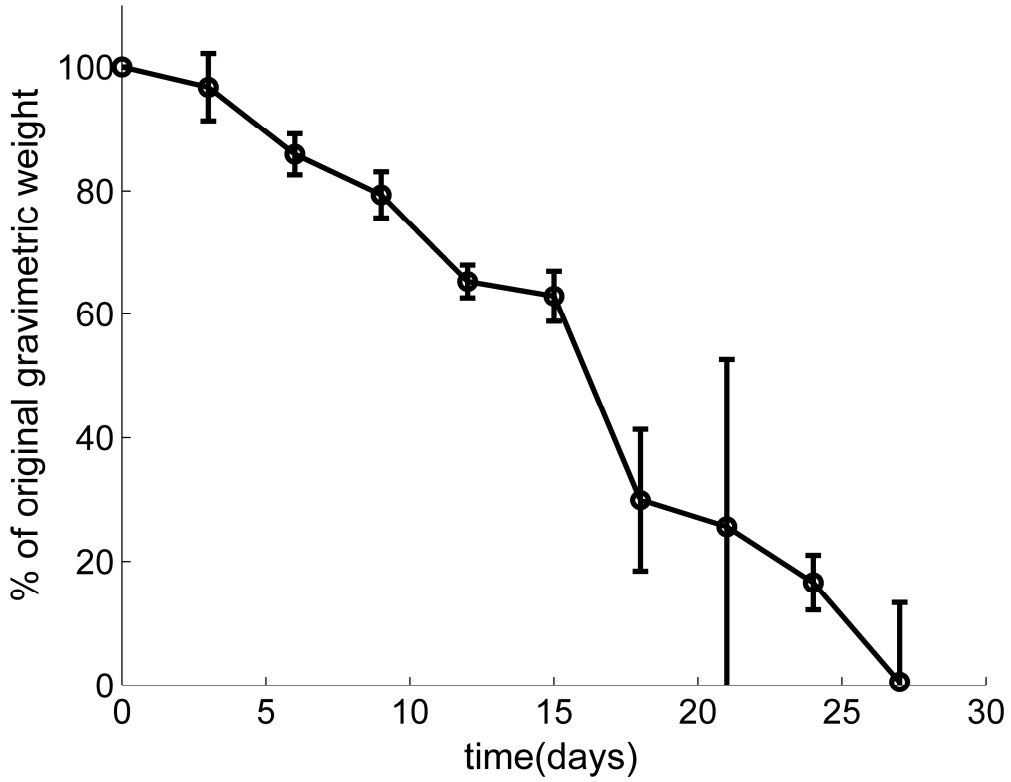

Figure 2.8. Gravimetric weight loss of PLGA scaffolds as a function of time. Error bars represent the standard deviation of three replicates.

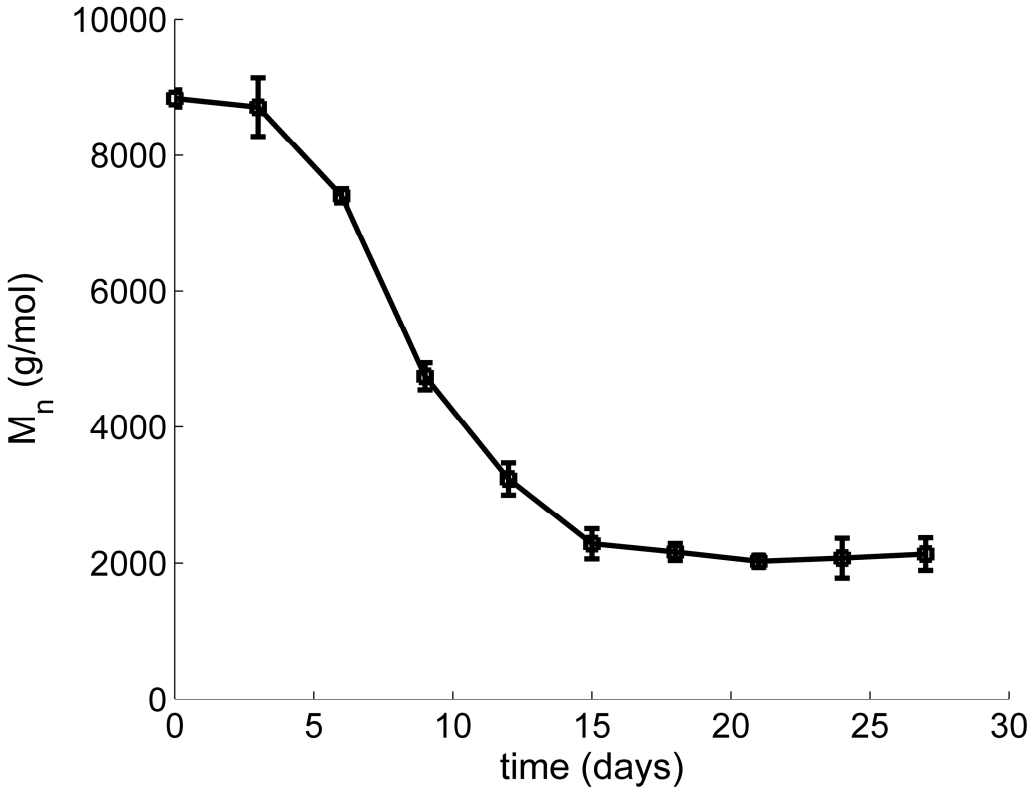

Figure 2.9. Molecular weight loss of the PLGA scaffolds as a function of time. Error bars represent the standard deviation of three replicates.

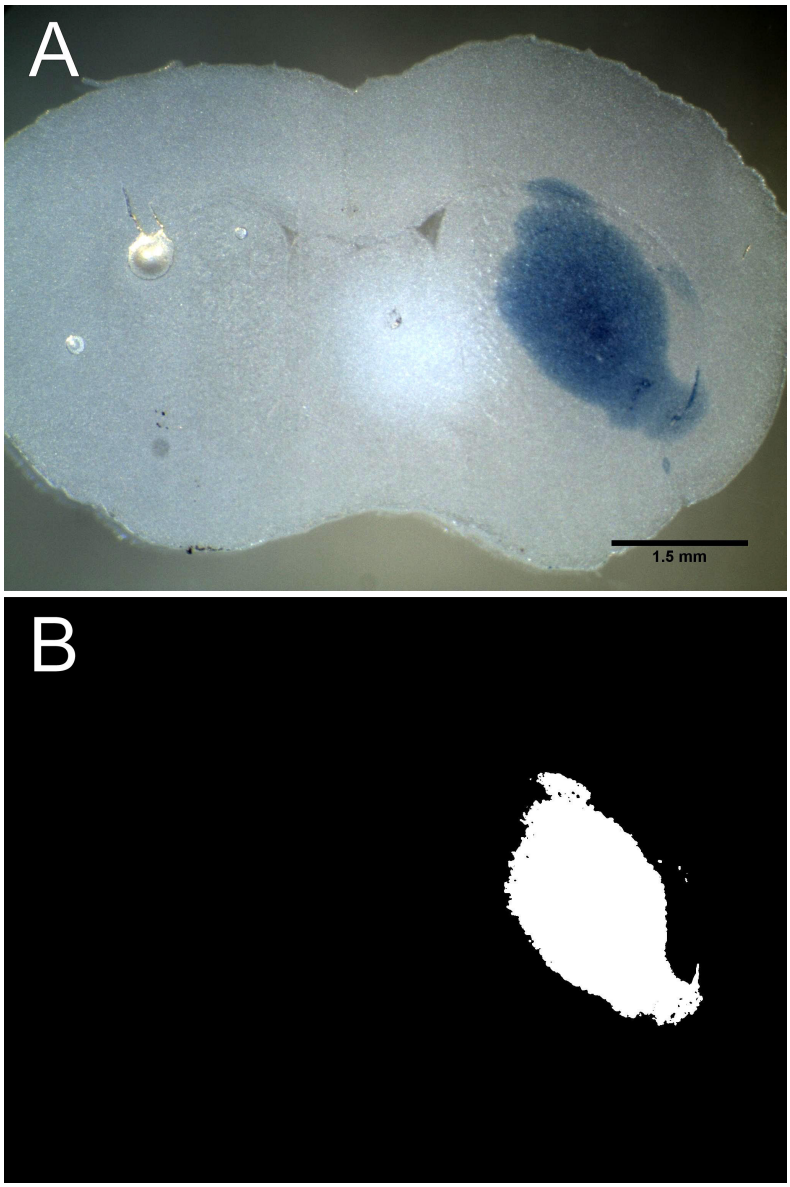

Figure 2.10. Photograph of 20µm thick section of mouse brain tissue showing Evan's Blue distribution (A), and the corresponding binary image that was used to calculate the volume of distribution as part of a series of sections (B).

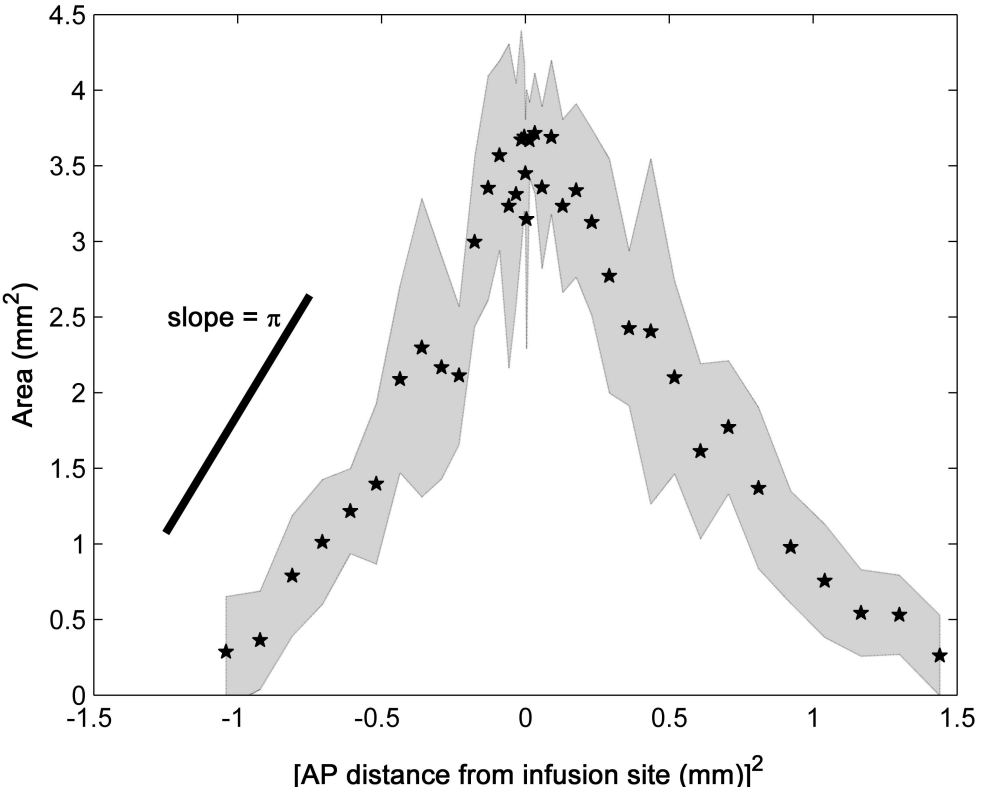

Figure 2.11. The average area of dye distribution in each brain section as a function of the square of the distance from the infusion site. The shaded region represents the standard deviation of the data (n = 5). A line with slope π is shown for reference. Areas of the plot with a slope equal to $\pm\pi$ correspond to a region where the distribution is isotropic. Deviations from this slope indicate anisotropic distributions.

square of the distance from the infusion site. If the dye distribution volume can be represented as a body of revolution around an axis in the anterioposterior (AP) direction the data presented in Figure 2.11 should fall on a straight line. If the distribution was a perfect sphere, the slope of the line would have slope π. Areas of the plot in Figure 2.11 with a slope equal to $\pm\pi$ correspond to regions where the distribution is isotropic. Deviations from this slope indicate regions of anisotropic distribution.

2.4 Discussion

The parylene microfluidic devices in this study were capable of infusing fluids in mouse striatum at flow rates that are relevant for convection enhanced delivery. Although the *in vivo* infusion rate obtained in this study of 0.09µl/min is low when compared with flow rates used in CED studies in humans (e.g. 2-12µl/min, [18-24], it is comparable to flow rates used by other groups that have studied CED in mice [49]. In this study, our final flow rate was limited by backflow. As shown by Morrison *et al* [26], the length of backflow along the outside of a needle or catheter is directly proportional to the volumetric flow rate imposed and the radius of the infusion catheter. In our case, using a higher flow rate would have caused the backflow to extend further along the outside of the device where it would reach the corpus callosum. This is due to the small size of the striatum of C57BL/6 mice where the distance between the tip of the inserted parylene device and the corpus callosum is approximately 1.6mm [50]. A device with a longer shank (e.g. 5mm) could be used in rats at higher infusion rates without incurring backflow. In any event, these data show that the parylene/PLGA system is capable of delivering fluid in a controlled and reproducible way. The ratio of the volume distributed (V_d) to the volume infused (V_i)

was 5.17 (n = 5), with a standard deviation of 0.36 (6.9% of the mean). This value is close to the theoretical value obtained for the free volume of the tissue given a porosity of 0.2 [51], which suggests that the parylene/PLGA system distributed all of the infused fluid to the available extracellular space of the tissue. Furthermore, the results presented in Figure 2.11 show that the distribution volume closely approximates the ideal spherical distribution associated with infusion from a point source.

The slight increase in size of the scaffolds when compared with that of the original silicon master is likely due to thermal expansion and pressure induced deformation of the PDMS mold during hot embossing. This effect was also observed by Yang *et al* [47].

The degradation time of the scaffolds in this study was determined *in vitro* to be 27 days, which was consistent with the manufacturers reported value (3-4 weeks). Grayson *et al* [48] found that the sample size affected its degradation time; larger samples were subject to bulk degradation, which accelerated their degradation compared with smaller samples that degraded primarily by surface erosion. In our case the scaffolds were large enough to undergo bulk degradation and therefore exhibited the manufacturer's reported degradation time.

PLGA structures have a long history of use in controlled release drug delivery devices [52] and their release characteristics have been well characterized. The insertion scaffolds could easily be loaded with drugs that might influence the local tissue to improve the effectiveness of the CED protocol, e.g. the controlled release of dexamethasone to mediate inflammation [53, 54]. To date, we have successfully loaded the PLGA scaffolds with up to 15wt% dexamethasone to examine the effect of local diffusive release of drug on the chronic performance of the parylene devices. Also, the degradation time of the scaffolds could be readily adjusted by changing the

molecular weight of the PLGA, by changing the end group, or by changing the lactide to glycolide ratio. This, in turn, could be used to control the duration of any local controlled release, which makes this a promisingly tunable system.

This study also shows that a flexible microdevice can be inserted into tissue using an external PLGA scaffold to stiffen the probe. The method presented here may be of use to researchers developing flexible neural electrodes for chronic applications. Takeuchi *et al* [55] used poly(ethylene glycol) (PEG) as a stiffening agent for flexible neural probes. In their technique a fluidic channel on the device is backfilled with molten PEG, which solidifies and stiffens the device enough to allow it to be inserted into tissue. The PEG then dissolves once the device is implanted. However, their devices were tested in the cortex of rats, so it is unclear whether the PEG is rigid enough to allow the devices to be inserted accurately into deep tissue structures. Furthermore, their method requires the implantable device to have a relatively large fluidic channel that can be backfilled with molten PEG. The use of an external PLGA scaffold would not require a fluidic channel if recording/stimulating electrodes were all that were needed, which would simplify the fabrication. Moreover, the dichloromethane application step is not required if infusions are not being performed, further simplifying the use of this system.

2.5 Conclusions

The results of this study show that it is possible to insert flexible polymeric devices into neurological tissue, and to use these devices to deliver fluid in a controlled and reproducible manner. This suggests that these devices could be suitable for use in chronic studies of convection enhanced delivery. Also, this is a straightforward technique, which could be easily used to implant other types of flexible neural

microprobes.

Although this system was conceived to exhibit improved chronic performance over conventional needles and catheters, characterizing and verifying that the system was capable of penetrating animal tissue and delivering fluid acutely and in a controlled way is a critical first step.

Future work on this system will compare the long term performance and biocompatibility of the parylene/PLGA system in chronic implants (with and without local diffusive delivery of therapeutics from the scaffolds), with those of silicon microprobes and conventional catheters. The devices will also be lengthened to permit their use in larger rodent models.

CHAPTER 3

REAL TIME STUDIES OF PERIVASCULAR TRANSPORT OF NANOPARTICLES IN THE RAT CORTEX

3.1 Introduction

Convection enhanced delivery (CED) is a promising technique for delivering drugs that do not readily cross the blood brain barrier to neural tissue. In this technique, a solution containing the drug is injected into the brain using a small needle or catheter. The transport is driven by pressure gradients rather than concentration gradients (as is the case for diffusive delivery from an implant or other reservoir), and therefore the drugs are able to penetrate further into the tissue [9]. Since CED is most likely to be used to deliver therapeutics that are too large to cross the BBB, such as nanoparticles, liposomes, proteins, and viral vectors, it is essential to fully understand how these large constructs are transported through tissue. This is important in planning future CED protocols to minimize leakage of therapeutics away from diseased areas into healthy tissue. Unanticipated leakage can cause serious side-effects and also negatively impact the efficacy of the therapy, and has been one of the major drawbacks associated with CED in clinical trials [19]. The difficulty in controlling the infusate distribution is due to the inhomogeneous nature of brain tissue, which contains regions of varying permeability such as ventricles, white and gray matter, and necrotic areas within diseased tissue. CED studies of large therapeutics suggest that perivascular spaces may also influence the distribution of infusates by providing high permeability paths for fluid to move through the brain.

Perivascular spaces are extensions of the sub-arachnoid space that surround arterial and venous blood vessels which penetrate the brain down to the level of capillaries. For many years they have been studied for their role in the bulk flow of cerebrospinal fluid (CSF) through the brain and in solute transport through the central nervous system [56-61]. These studies demonstrated that tracers injected into the subarachnoid space distributed through the brain parenchyma via perivascular spaces.

Cserr and Ostrach [62] examined how a bolus infusion of blue dextran in the striatum of a rat dispersed through the brain over 24 hours. They found that the dye spread over a greater distance than would be possible through pure diffusion, and noted that the tracer travelled along perivascular spaces away from the infusion site. Furthermore, they demonstrated that when edema around the insertion site was eliminated (by either administering an anti-inflamatory or waiting 7 days after inserting the cannula before infusion), that the dye remained localized around the insertion site and did not get widely distributed throughout the brain. This suggests that perivascular spaces act as conduits for elimination of excess fluid from the brain.

Studies examining CED of liposomes and viral vectors have observed evidence of perivascular transport in rodents and primates [63-67]. Mamot and coworkers [66] co-infused liposomes and mannitol into rodent brains and intracranial and flank implanted xenograft tumors. During post-mortem histological examination they observed that the liposomes were distributed along the blood vessels of the tumors. Krauze *et al* [65] infused gadolinium and rhodamine loaded liposomes into the putamen of non-human primates while performing MRI and magnetic resonance angiography (MRA). Co-localizing the images from the MRI and MRA studies showed that the liposomes were travelling along large blood vessels in the brain, and histological examination showed that the liposomes were localized in the perivascular space of these vessels. Hadaczek and colleagues [64] infused viral vectors, fluorescent

liposomes, and BSA into the striatum of rats with high, low, and no heart-rate. They saw evidence of perivascular transport along vessels, and observed that heart rate was directly correlated to the final distribution volume of the infusates. They suggest that the passage of infusates through the brain may be aided by "perivascular pumping" through the perivascular spaces driven by pulsations of the vessel walls.

Although these works demonstrated that large therapeutics tend to accumulate in the perivascular space, it is difficult to garner knowledge about the dynamics of how the drugs pass through tissue. Studies using MRI can track the distribution of paramagnetically labeled infusates in real time, but they lack the spatial resolution required for examining dynamic behavior for all but the largest blood vessels of the brain. In this study we used two-photon excited fluorescence (2PEF) microscopy to examine how nanoparticles are transported through the rat cortex during CED. This technique allowed us to monitor the nanoparticle distribution in real time, with micrometer-scale resolution.

Two-photon excited fluorescence microscopy allows fluorescence imaging with intrinsic optical sectioning deep inside scattering specimens with diffraction-limited resolution [68]. Briefly, a femtosecond laser pulse is tightly focused inside a specimen that has been labeled with a fluorescent molecule that does not linearly absorb at the wavelength of the femtosecond laser. At the laser focus, the laser intensity can become high enough to induce two-photon excitation of the fluorescent molecule. Because the excitation is nonlinear, the resulting fluorescence is only produced in the focal volume where the laser intensity is high. The fluorescence intensity is then recorded as the position of the laser focus is scanned throughout the specimen forming a three-dimensional map of the distribution of the fluorescent label. In addition, because photoexcitation occurs only at the laser focus, photobleaching of fluorescent dyes and photodamage to the sample are reduced significantly compared to

linear imaging techniques [69].

2PEF microscopy is well suited to *in vivo* imaging, especially deep inside highly scattering specimens. In widefield or confocal fluorescence microscopy, the fluorescence must be imaged to a camera or to a pinhole, respectively. Scattering of the fluorescence light leads to an unwanted background in widefield microscopy and to decreased signal strength in confocal microscopy. In 2PEF microscopy, however, because all the fluorescence originates from the focal volume, it need only be detected in order to contribute to the signal, not imaged to a camera or pinhole. Thus fluorescence that is scattered on the way to the detector still contributes to image formation, and does not produce an unwanted background. This tolerance to scattering of the fluorescence allows imaging deep into scattering samples. The imaging depth is ultimately limited by scattering of the femtosecond laser beam. In practice, one can image 500μm or more beneath the surface of typical tissues (brain, skin, kidney, etc) without loss of image resolution [68, 70-72].

In this study, we infused fluorescent nanoparticles into the cortex of rats using microfluidic delivery devices. During infusions, we captured 2PEF images at a fixed location in the brain which was a known distance from the tip of the microfluidic probe. By noting where in our imaging plane nanoparticles first appeared we could determine whether the particles were transported primarily through the perivascular spaces or through the extracellular space (ECS). Furthermore, because both the distance traveled by the nanoparticles and the elapsed time were measured, we were able to determine the primary transport mechanism by comparison to the characteristic times for convective and diffusive transport. We found that the nanoparticles were transported through the perivascular spaces much more readily than through the bulk extracellular space of the brain. These results show that delivery of large (50-150nm diameter) therapeutic constructs to neural tissue using CED requires careful

consideration of the vasculature of the target area to minimize the escape of therapeutics from the disease afflicted regions, and to maximize the effectiveness of the infused drug.

3.2 Materials and Methods

3.2.1 Nanoparticle Preparation

Carboxylate-modified fluorescent nanoparticle stock solutions (24 and 100nm FluoSpheres, Invitrogen, Carlsbad CA) were sonicated for 15 minutes before being diluted to 0.02wt% solids in 1% BSA (Sigma-Aldrich, St. Loius MO) in phosphate buffered saline (approximately 10^{13} particles/ml and 10^{11} particles/ml for 24nm and 100nm, respectively). The nanoparticle solutions were then gently rotated using a laboratory rotisserie at room temperature for 4 hours. This treatment reduced the surface charge of the nanoparticles and therefore reduced non-specific binding of the particles to the extra cellular matrix [73].

The size and surface charge of the nanoparticles were determined before and after BSA incubation via dynamic light scattering and laser Doppler measurements of particle mobility under electrophoresis (Zetasizer Nano, Malvern Instruments Ltd., UK), respectively.

3.2.2 Microfluidic Device Preparation

Silicon based microfluidic devices were fabricated as previously described [30]. The devices had a 5mm long insertable shank with a 100×100μm cross-section. The microfluidic probes were attached to 150mm long borosilicate micropipettes (1mm

OD, 0.58mm ID) (World Precision Instruments Inc., Sarasota FL) with two-part epoxy (Epoxy 907, Miller-Stephenson, Danbury CT). The devices were backfilled with the nanoparticle solution under vacuum, before the glass capillary was filled via a syringe with a custom MicroFil tip (World Precision Instruments Inc., Sarasota FL). The micropipette served as the fluidic reservoir for the microfluidic device. The proximal end of the glass micropipette was connected to a programmable pressure injector (PM8000, World Precision Instruments Inc.) using a micro-electrode holder. To infuse fluid using the microfluidic device a constant pressure was applied to the fluidic reservoir in the micropipette via the pressure injector.

3.2.3 *In Vivo* Nanoparticle Infusions

Five male Sprague Dawley rats (weighing 283 - 370g) were anesthetized via intra-peritoneal injection of 30wt% urethane in DI water (urethane dose of 150mg urethane/100g body weight). Animals were then secured in a stereotaxic frame and an incision was made in the skin along the dorsal midline to expose the skull. A large craniotomy (~1cm diameter) was opened in the left parietal bone using a dental drill and the dura was removed using a fine hook. The vasculature was labeled via tail vein injection of fluorescein isothiocyanate (FITC) conjugated to 2MD dextran or tetramethylrhodamine conjugated to 6kDa dextran. The tail vein injection fluorescently labels the blood serum, allowing the blood vessels of the cortex to be visualized under 2PEF. If red nanoparticles were used, the blood vessels were labeled with green FITC-dextran, and conversely, if green particles were used the vasculature was labeled with red tetramethylrhodamine-dextran.

Animals were then transferred to the stage of the 2PEF microscope, and microfluidic probes were inserted 1mm into the cortex at a downward angle of 15°

using a micromanipulator. The tissue was allowed to equilibrate for at least 2 mins before infusions were initiated. During this time, imaging stacks were collected in the dorsoventral direction to map the vasculature and to determine a suitable imaging location for monitoring the nanoparticle distribution during the infusion. The imaging location selected was the level directly above the probe that had the greatest number of vertically oriented blood vessels (i.e. penetrating arterioles and ascending venules) that intersected the imaging frame. A schematic of the experimental set-up is shown in Figure 3.1. Infusions were started at a driving pressure of 0.5psi, and the infusion pressure was increased at a rate of 0.1psi/30sec to a final pressure of 1psi. This resulted in a flow rate of approximately 0.1µl/min. 2PEF imaging frames were captured at 3.39 frames/second throughout the infusions and examined for the location of the first appearance of nanoparticle fluorescence (in perivascular spaces or in ECS). After an infusion was complete, the imaging area could be scanned through the tissue in three dimensions to map the final nanoparticle distribution (up to a maximum depth of approximately 700µm below the brain surface).

2PEF images were taken on a microscope of local design using 100fs, 76MHz laser pulses from a titanium:sapphire oscillator (Mira-HP, Coherent, Santa Clara CA) pumped by a continuous wave laser (Verdi-V18, Coherent, Santa Clara CA). Excitation wavelengths were centered at 810nm and 850nm for yellow-green and red fluorescent nanoparticles respectively. Detection filters were 525/70nm and 615/70nm. Low magnification images were taken with a 0.2-NA, 4x air objective (Olympus). High magnification images used a 0.95NA, 20x water immersion objective (Olympus) with a 2mm working distance.

All procedures were carried out in accordance with the Cornell University Institutional Animal Care and Use Committee guidelines and regulations.

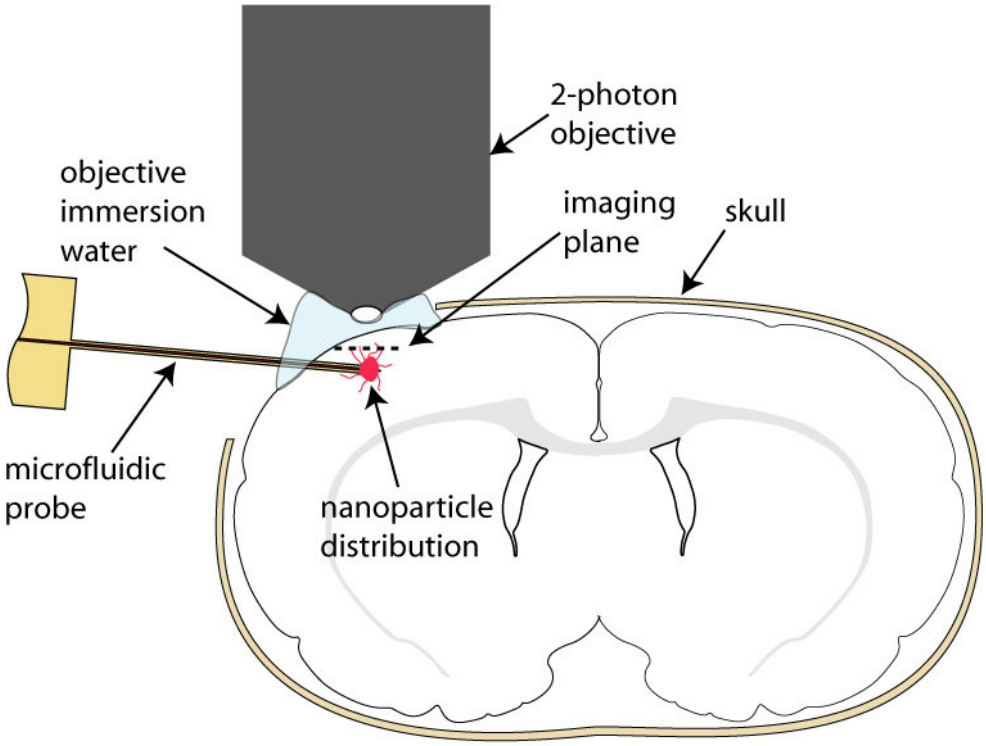

Figure 3.1. Experimental set-up for real-time 2-photon imaging of perivascular transport of nanoparticles.

3.3 Results and Discussion

3.3.1 Nanoparticle Characterization

In this study we used 2PEF microscopy to examine in real time how BSA coated polystyrene fluorescent nanoparticles are transported through rat cortex during CED. The measured diameter of the particles as received from the manufacturer were 44.5±1.6nm and 134.8±0.6nm for the small (24nm nominal diameter) and large (100nm nominal diameter) respectively. This increase is possibly due to slight aggregation of the sample combined with the fact that dynamic light scattering measurements can be skewed by the presence of a few large particles. After incubation with BSA, the measured diameter of the particles increased to 62.1±3.9nm and 152.3±2.7nm for the small and large nanoparticles respectively. The average increase in diameter of the particles is 17.6nm, which is in good agreement with the hydrodynamic diameter of BSA (7.2nm [74]). The zeta potentials of the nanoparticles before BSA coating were -36.8±2.8mV and -38.6±3.6mV for the small and large particles respectively. After BSA coating the zeta potentials were -10.8±3.4mV for the small, and -11.4±2.5mV for the large particles. As anticipated, the surface charge was decreased by the presence of BSA.

3.3.2 Nanoparticle transport in the rat cortex

Microfluidic probes were inserted 1mm into the cortex of rats at a downward angle of approximately 15° and nanoparticle solutions were infused at a flowrate of 0.1µl/min. During infusions imaging frames were captured at a fixed level above the probe outlet but below the brain surface. We found that nanoparticles of both sizes preferentially

Table 3.1. Summary of the results of the nanoparticle infusions, giving the size of the particle infused, the distance from the probe tip to the imaging plane, and the time taken for the particles to appear in the imaging frame.

Infusion	Nominal particle size (nm)	Distance to imaging plane (μm)	Time to arrival at imaging plane (s)
1	24	243	13
2	24	290	200
3	24	220	14
4	24	360	30
5	24	92	No NP fluorescence seen
6	100	300	110
7	100	280	No NP fluorescence seen

traveled along perivascular spaces rather than through the ECS. Table 3.1 summarizes the experimental conditions for each infusion, giving the particle size, the distance from the probe outlet to the imaging plane, and the time taken for nanoparticles to reach the imaging plane.

3.3.2.1 24nm nanoparticle transport

Five infusions of 24nm BSA coated nanoparticles were performed under real time monitoring via 2PEF microscopy (infusions 1-5, Table 3.1). In four of these infusions the first appearance of nanoparticles at the imaging plane was in the perivascular spaces of vessels (1-4, Table 3.1), followed by a gradual filling in of fluorescence in the extracellular space between the vessels (Figure 3.2). The nanoparticles did not spread into the tissue in a perpendicular direction to the perivascular space in an appreciable amount on the time scale of our experiments. The fluorescence in the perivascular space was primarily constrained around arterioles and

Figure 3.2. Time course showing transport of red fluorescent nanoparticles (24nm nominal diameter) through perivascular spaces during CED. Images were captured 243μm above the outlet of the microfluidic device. Image A is at infusion time = 0s; B = 30s; C = 90s; D = 150s. Note appearance of nanoparticles around vessels in panel B, and gradual filling in of background ECS in panels C and D.

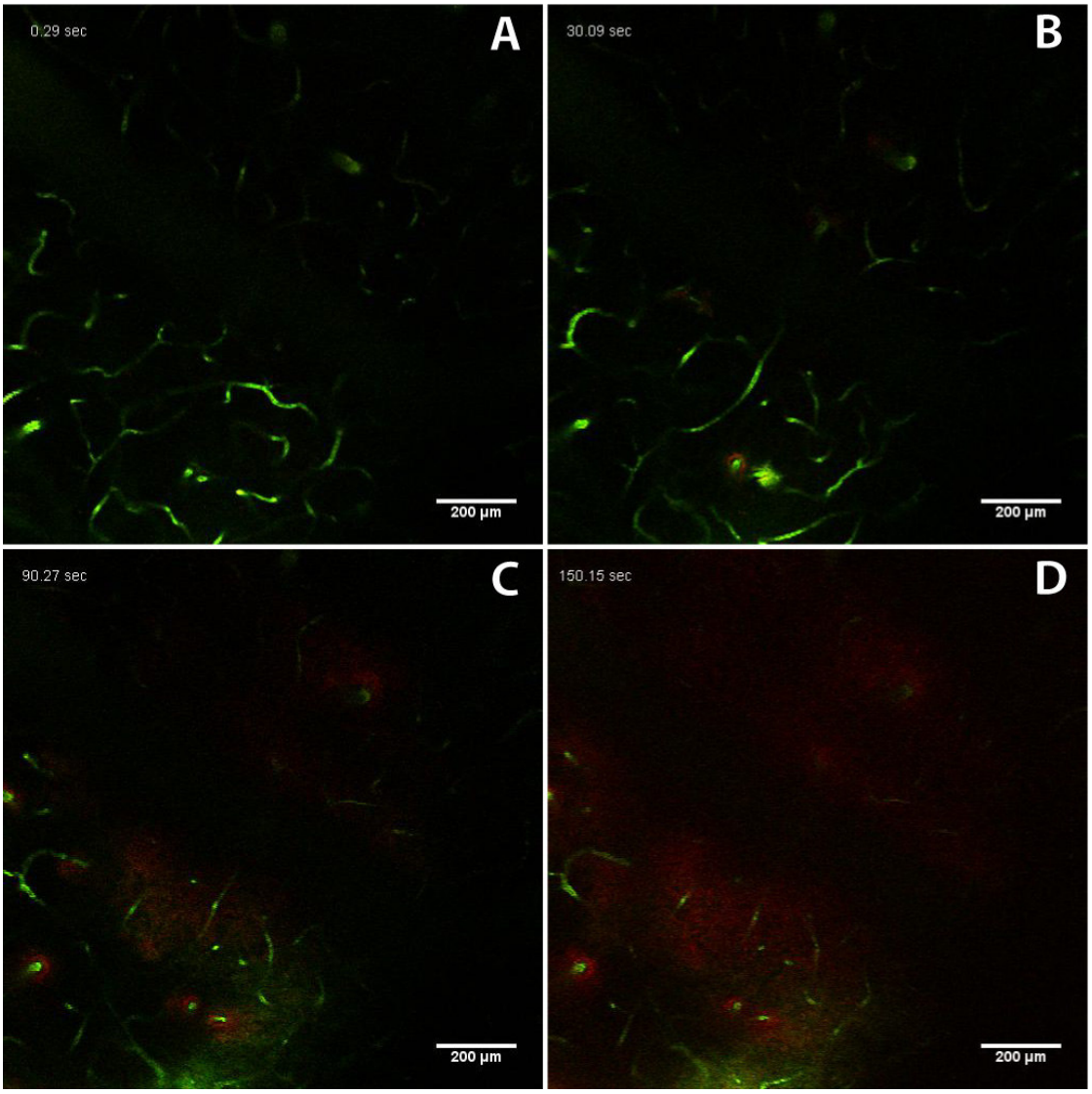
0.29 sec
A
200 µm
30.09 sec
B
200 µm
90.27 sec
C
200 µm
150.15 sec
D
200 µm

venules, with a small amount extending along capillaries for a short distance (~40-50μm) after branching from larger vessels (Figure 3.3).

If we consider the infusion to be an ideal infusion into a porous medium from a point source, we can determine the characteristic time for the convective front of infused fluid to reach a radial distance from the point source, r, to be:

$$t_c = \frac{4\pi\phi}{3Q} r^3 \tag{1}$$

where, t_c is the characteristic time for convection, Q is the flow rate of the infusion, and ϕ is the porosity of brain tissue (~0.2 [51]). Using this equation with a flow rate of 0.1μl/min we find that the characteristic time for a convective front of fluid to reach the imaging plane of our experiments (a distance of 220-360μm) is between 5.4 and 23.5 seconds.

The characteristic time for a particle to diffuse a distance, r, through brain tissue can be determined from:

$$t_d = \frac{r^2}{D^*} \tag{2}$$

where, t_d is the characteristic time for diffusion, and D^* is the effective diffusion coefficient of the particle in the tissue.

$$D^* = \frac{D}{\tau^2} \tag{3}$$

where, D is the diffusion coefficient of the particle in a free medium, and τ is the tortuosity of the extra cellular space of the brain (τ ~ 2, [75, 76]). The diffusion

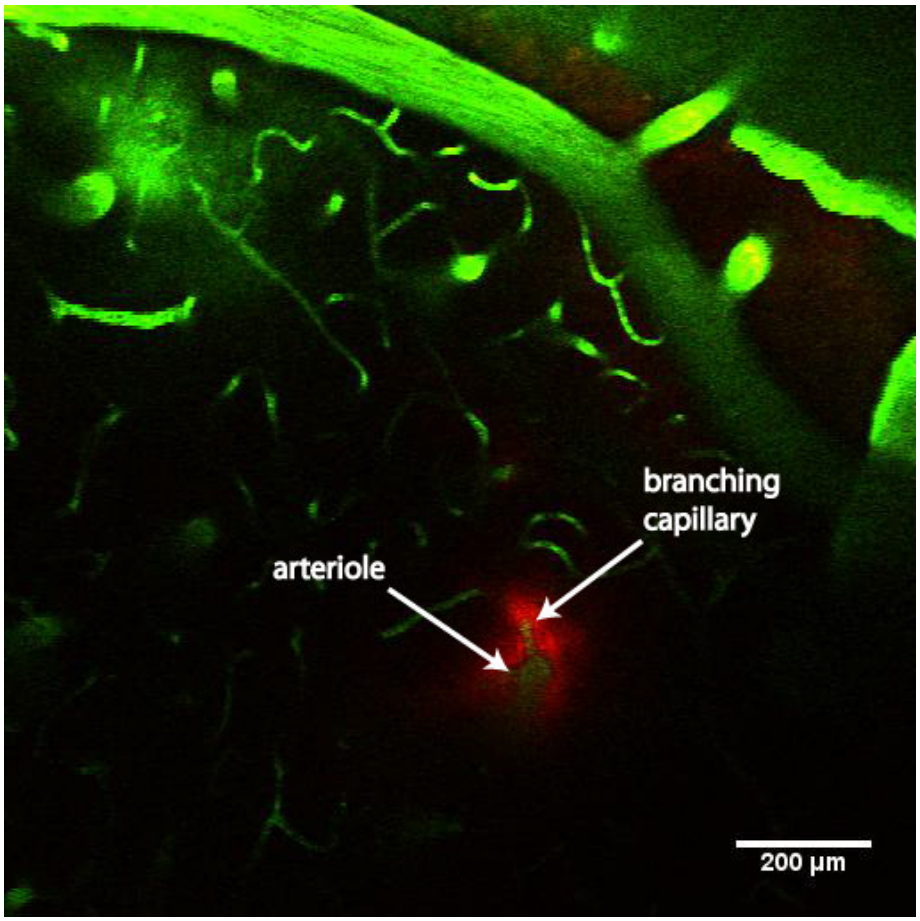

Figure 3.3. Image showing 24 nm nanoparticles in perivascular spaces around branching capillary. BSA-coated red nanoparticles were infused into the rat cortex, and the vasculature was labeled with fluorescein. The image shows the distribution of red fluorescent nanoparticle around a branching capillary (~10µm diameter). Nanoparticles extend for ~50µm along the capillary after branching from arteriole.

coefficient of a particle in a free medium (e.g. water) can be estimated from the Stokes-Einstein equation:

$$D = \frac{kT}{3\pi d_H \eta} \tag{4}$$

where, k is the Boltzmann constant (1.38065×10^{-23} $m^2kgs^{-2}K^{-1}$), T is the temperature in Kelvin (310 K), d_H is the hydrodynamic diameter of the particle (24nm for the best possible case), and η is the viscosity of the free medium at the temperature T (6.9152×10^{-4} Pa.s [76]). Using these equations we can determine that the characteristic time required for a particle to reach our imaging plane from the outlet of the probe (220-360μm) through pure diffusion is between 90 and 241 minutes.

In our experiments, the time taken for fluorescence to appear in the imaging plane ranged from 13 to 200s (infusions 1-4, Table 3.1). From these data we can infer that the nanoparticles were transported through the tissue primarily via convection. The possible reasons that time for the nanoparticles to appear *in vivo* were longer than the characteristic convective times of 5.4 – 23.5 seconds are numerous.

In the infusion that took 200s (infusion 2), post-infusion analysis showed that the majority of the fluid had backflowed along the insertion track of the microfluidic device due to a mechanical disturbance to the microfluidic probe, which resulted in tearing of the tissue in the area of the device tip. This meant that the bulk of the fluid was transported along the high permeability device track, leaving little driving pressure to force the fluid through the ECS to the perivascular space. The perivascular transport observed at the fixed imaging plane during the infusion was along a vessel that passed close to the microfluidic probe in a more ventral plane, and thereby intersected the backflowing nanoparticles.

For the other infusions (1, 3, 4) the time taken for nanoparticles to appear at the imaging plane ranged from 13s for infusion 3 (220μm above probe outlet) to 30s for infusion 4 (360μm above probe) after the infusion began. In these cases the reasons for the longer time are most likely that the nanoparticles do not undergo ideal convective transport through the tissue, and that the perivascular spaces do not in general pass directly from probe outlet to imaging plane, but follow a longer and more circuitous path. Furthermore, the distance that the nanoparticles must travel through the ECS before reaching the perivascular space of the vessel that intersects the fixed imaging plane is different in each infusion, and unknown. The expression given above for the characteristic convection time (Equation 1) assumes that the volume of fluid infused occupies the free volume of the tissue. In the case of our infusions, it is very likely that the nanoparticles undergo hindered transport through the extracellular space, considering that their diameter is on the same order as the estimated pore size of the extracellular matrix (38 – 64nm [76]). Previous research in our group using these nanoparticles found that the ratio of the volume of nanoparticles distributed through the grey matter of the rat striatum to the volume of nanoparticle solution infused was 0.35 [73], rather than a value close to 5 as one would expect if all the infused fluid filled the extracellular space of the tissue. This suggests that the solid nanoparticles pass through the tissue more slowly than the fluid by a factor of approximately 14. If this is the case, it implies that the time taken for nanoparticles to reach the imaging plane by transport through the ECS would be on the order of 75 – 330 seconds for distances of 220 – 360μm. These values are on the same time-scale as those observed during our infusions for the first appearance of nanoparticles in the ECS at our imaging plane. For example, in infusion 1 (Figure 3.2) the first appearance of nanoparticles at our fixed imaging plane (243μm above the channel outlet) occurred after approximately 55s.

In infusion 5, nanoparticles were seen to transport through the extra cellular space and no perivascular transport was observed in the imaging plane during the infusion. However, post-infusion imaging showed that nanoparticles had localized in perivascular spaces in a more dorsal plane than the imaging plane used during the infusion. This suggests that there were no highly permeable perivascular spaces in the fixed imaging plane used during the infusion, but that once the convective front of the nanoparticle distribution reached the perivascular spaces of larger vessels, these conduits of higher permeability then became the preferred path for nanoparticle transport.

In infusion 4, we observed the nanoparticles traveling along a vessel that lay in the imaging plane at a distance of 360μm above the tip of the probe (Figure 3.4). This allowed us to measure the speed of the nanoparticle distribution along the vessel wall to be 0.026mm/s. Measuring the diameter of the blood vessel (0.03mm) and nanoparticle distribution (0.049mm) allows us to determine the cross sectional area of the perivascular space to be 1.18×10^{-3} mm^2 (assuming that the perivascular space is a circular annulus around the vessel, and that the nanoparticle distribution occupies the entire perivascular space). Multiplying this area by the speed of the nanoparticle flow through the perivascular space gives a flow rate in the annulus of 1.84×10^{-3} μl/min. The velocity of the convective fluid front through a porous medium can be found from:

$$v(r) = \frac{Q}{4\pi\phi r^2} \tag{5}$$

where, $v(r)$ is the velocity as a function of radial distance from a fluid source, Q is the volumetric flow rate of the fluid source, ϕ is the porosity of the tissue, and r is the

Figure 3.4. Time course showing transport of green fluorescent nanoparticles (24nm nominal diameter) along vessel in imaging plane. The vasculature is labeled with tetramethylrhodamine. Times represent duration of the infusion (A = 14.5s, B = 34.8s, C = 41.0s and D = 65.5s). Images were captured at a plane 360µm above the outlet of the microfluidic probe, 240µm below the surface of the brain.

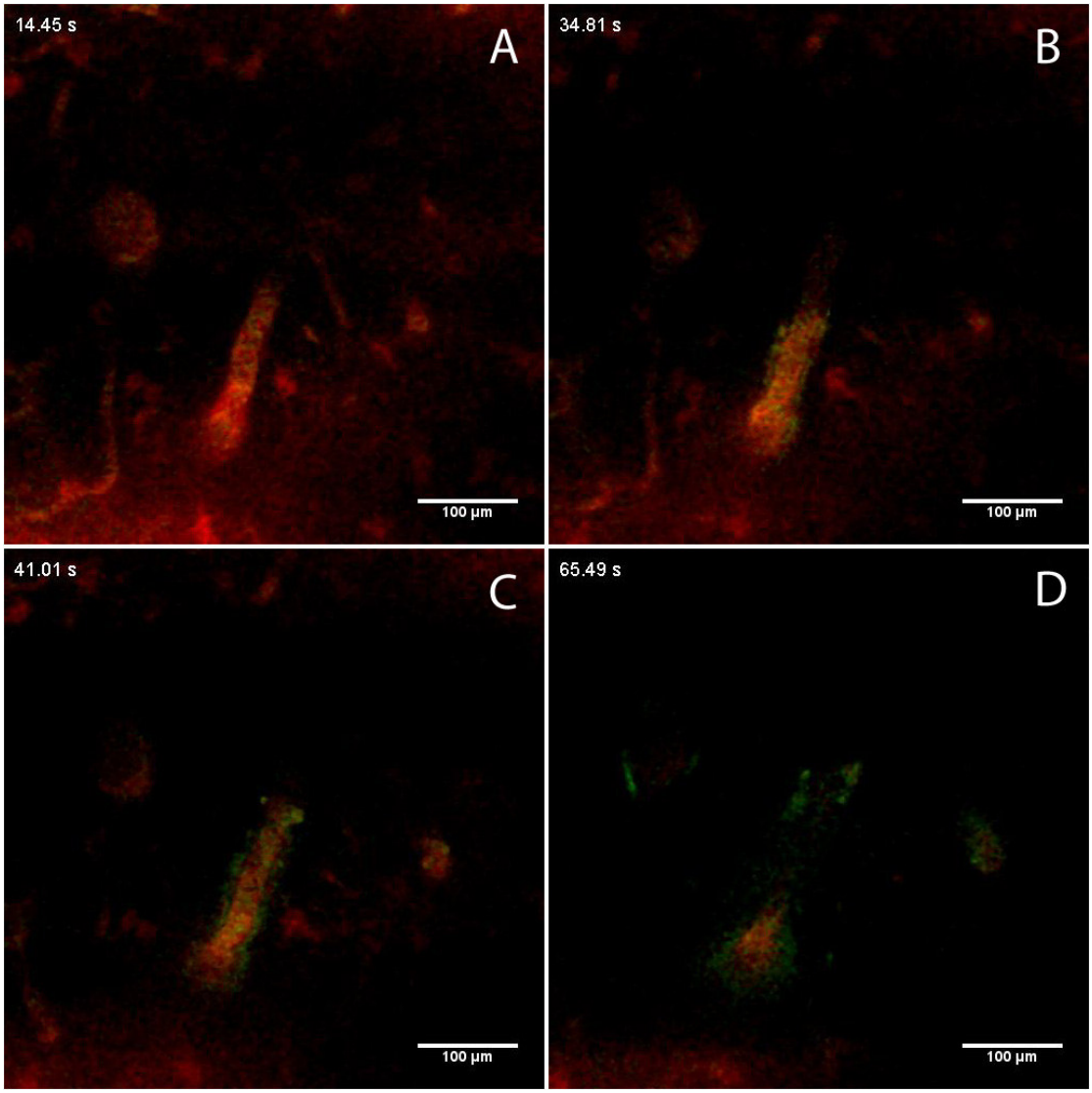
14.45 s
A
100 µm
34.81 s
B
100 µm
41.01 s
C
100 µm
65.49 s
D
100 µm

radial distance from the fluid source. Substituting a flow rate of 0.1μl/min and a distance of 360μm we find that the speed of a convective fluid front passing through the ECS is approximately 0.005mm/s, which is five times slower than the speed of nanoparticle transport we observed in the perivascular space of a vessel this distance from the channel outlet. However, this increase is to be expected, since at this radial distance from the probe, the flow is travelling through the perivascular spaces and not the larger surface area for flow assumed above in Equation 5. This result shows that perivascular spaces can provide a route for rapid egress of large constructs from target tissue volumes.

3.3.2.2 100nm nanoparticle transport

In the case of the 100nm nominal diameter nanoparticles, two infusions were performed. In infusion 6 we saw nanoparticles reach the imaging plane (a distance of 300μm) 110 seconds after the infusion was started, which was approximately 4 times longer than required for 24nm particles. In infusion 7, nanoparticles were not observed at the fixed imaging plane during the infusion, but post infusion analysis revealed that the particles followed the perivascular space of a vessel that passed close to the outlet of the microfluidic device but did not intersect the imaging frame at the level we were observing. In both cases, post-infusion imaging showed that the nanoparticles did not move through the ECS, and instead were constrained in the perivascular space of vessels (Figure 3.5). The long time taken for the nanoparticles to appear at the imaging plane is most likely due to the fact that the 100nm particles undergo greatly hindered transport through the ECS, since their diameter is approximately twice the average pore size of the extracellular matrix [76]. Once the nanoparticles reach the perivascular space there is little structure present to impede their motion [58]. This

Figure 3.5. Sections from a post-infusion stack in the dorsoventral direction, showing red fluorescent 100nm nanoparticles constrained in the perivascular space. Frame A is an optical section 50µm below the brain surface; B = 100µm; C = 150µm; D = 200µm. Images show that the nanoparticles are distributed in the perivascular space of the vessel over a distance of several hundred micrometers. The outlet of the microfluidic device was 550µm below the brain surface.

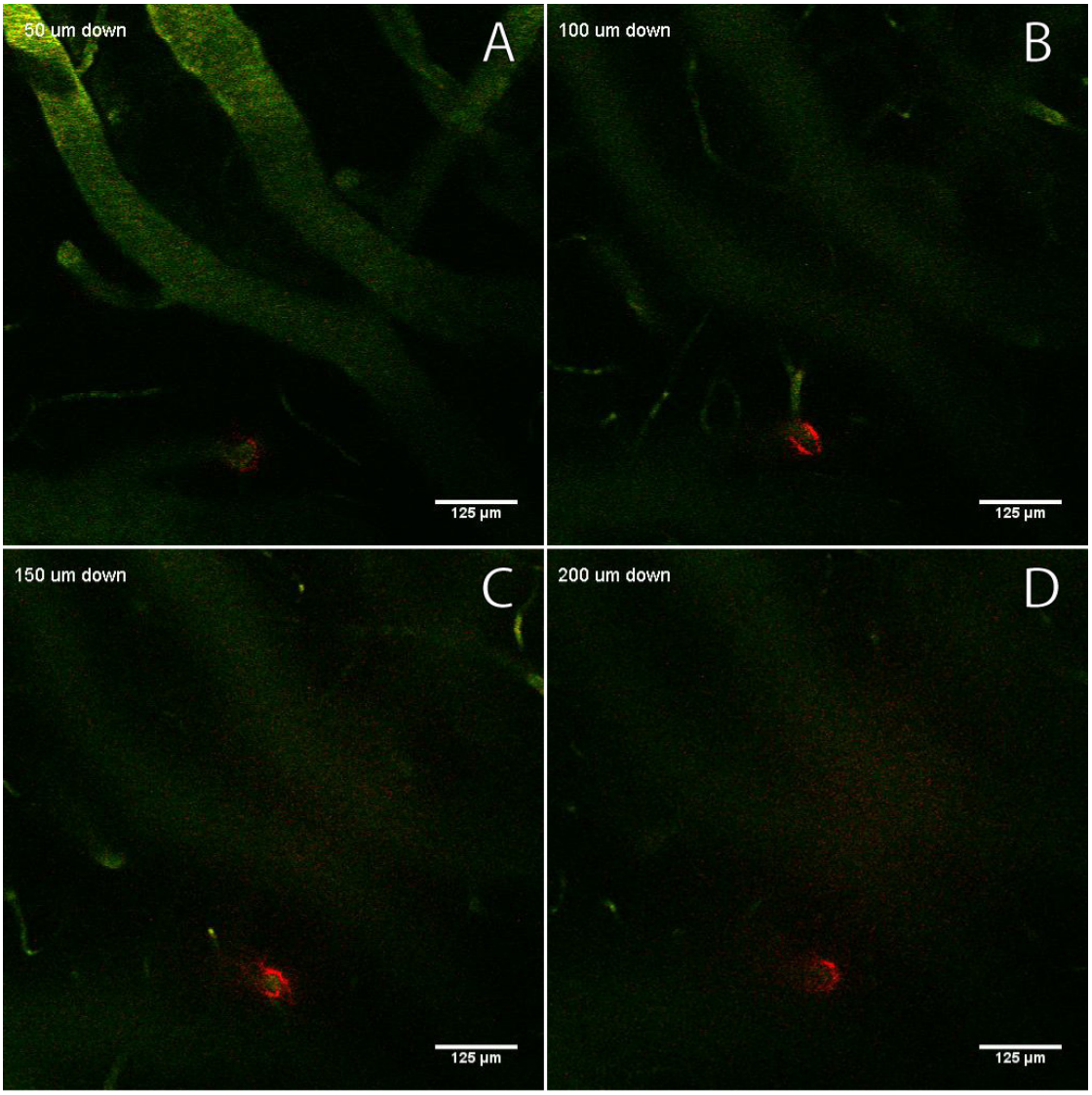
50 um down
A
125 µm
100 um down
B
125 µm
150 um down
C
125 µm
200 um down
D
125 µm

suggests that for particles much larger than the pore size of the ECM, perivascular spaces might be even more significant paths for transport through the central nervous system than for smaller particles that undergo less hindered transport in the ECM.

If a therapy involves delivering constructs that are going to undergo significantly hindered transport through the ECM to an area of the brain where perivascular spaces provide a high permeability path of egress to healthy tissue, it may be of use to increase the hydraulic permeability of the bulk extracellular space to reduce the likelihood that the particles will travel along the blood vessels to healthy tissue. This modification of the hydraulic permeability can be achieved through degrading or dilating the extra cellular matrix as demonstrated by Neeves and coworkers [73]. An alternative way to decrease the fraction of the therapeutic that escapes the target area through perivascular spaces would be to make the constructs smaller, thereby increasing the apparent permeability of the ECM seen by the particles.

3.4 Conclusions

In this study we used 2PEF microscopy to study the transport of fluorescent nanoparticles through the cortex of rats during convection enhanced delivery via microfluidic probes. The distributions of two different sizes of nanoparticles were examined. We observed that perivascular spaces in the area of the microfluidic device outlet can greatly affect the transport of the particles by providing high permeability conduits for fluid transport.

Furthermore, we noted that perivascular transport is dependent on the size of the particle involved. For smaller particles that can readily pass through the ECM the fraction of the infused particles that move through the perivascular spaces rather than

the ECS is lower than for large particles that undergo significantly hindered transport through the ECM.

From these results, it is clear that a thorough understanding of the vasculature of the target tissue and the physical properties of the construct being delivered are of critical importance in designing new CED protocols to reduce undesirable distributions and thereby maximize the effectiveness of the new therapies.

CHAPTER 4

ENDOVASCULAR MICROCATHETER FOR SELECTIVE INTRA-ARTERIAL CEREBRAL INJECTION OF SMALL ANIMALS

4.1 Introduction

It is estimated that 780,000 strokes occur in the United States every year. Of these, 600,000 are first attacks, and 180,000 are recurrent strokes. On average, someone in the United States suffers a stroke every 40 seconds. In terms of mortality, strokes accounted for 1 in every 16 deaths in the United States in 2004, which makes stroke the third leading cause of death behind heart disease and cancer. Stroke is also a major cause of long term disability. The American Heart Association estimates that the direct and indirect economic costs of stroke will total $65.5 billion in 2008 [77].

A stroke is a type of cardiovascular disease that occurs when part of the brain is starved of oxygen or nutrients due to a loss of blood flow. Brain cells in this blood deprived region die, resulting in neurological deficits or possibly death. There are two types of strokes: ischemic and hemorrhagic. Thirteen percent of stroke cases are hemorrhagic. These can be caused by leakage of blood from a vessel into the brain (intracerebral hemorrhage, 10% of total stroke cases), or by blood loss into the subarachnoid space between the arachnoid membrane and pia mater of the meninges (subarachnoid hemorrhage, accounting for 3% of total stroke incidences). Ischemic strokes account for the remaining 87% of all strokes and can be caused by thrombosis (formation of a clot in a blood vessel feeding the brain), embolism (migration of an obstruction from one part of the body into a vessel), or systemic hypoperfusion. This

work will focus on ischemic stroke.

In an acute ischemic stroke there exists a region of brain tissue that is exposed to significantly reduced blood flow. This region is known as the core infarct, and is rendered nonviable within minutes of the arterial occlusion. Surrounding this core ischemic volume is a region of tissue known as the "ischemic penumbra" that suffers from reduced blood flow, but remains viable and could possibly be salvaged. Treatments for acute ischemic stroke focus on saving the ischemic penumbra by reestablishing blood flow to this volume, and studies show that early recanalization of the occluded vessel mitigates the long term neurological deficits associated with acute ischemic stroke [78, 79].

However, recanalization is not without risks, including: cerebral hemorrhage [80-82], reocclusion [83], late secondary ischemic injury (the delayed development of ischemic injury after initial signs of recovery) [84-86], and the continuation of oligemic zones to infarction despite reperfusion [87]. Two widely used techniques to achieve revascularization of the ischemic penumbra are described below.

The most common therapy for ischemic stroke is the intravenous or intraarterial administration of recombinant tissue plasminogen activator (rt-PA). Mammalian blood has an intrinsic enzymatic system capable of dissolving blood clots known as the fibrinolytic enzyme system. This system contains a proenzyme, plasminogen, which can be converted to plasmin, a fibrin degrading enzyme [88]. rt-PA is a serine protease that cleaves the arginine-valine bond of plasminogen, resulting in the active proteolytic enzyme plasmin. rt-PA is relatively clot-specific in that its activity is enhanced approximately 400-fold when bound to fibrin. However, this thrombolytic drug is generally only administered to the patient within 3 hours of the onset of the stroke due to the 10-fold increase in risk of intracranial hemorrhage associated with the treatment [89]. Studies have shown that the median delay between

stroke onset and arrival at a hospital is between 3-6 hours [77]. As a result, although this treatment is effective, only 2-3% of stroke patients receive it due to the limited window for administration [90].

In August 2004, the FDA approved a new device for treatment of ischemic strokes that has a longer therapeutic time window. The Mechanical Embolus Removal in Cerebral Ischemia (MERCI) device consists of three parts: the retriever, the microcatheter, and the balloon guide catheter (BGC). The retriever consists of a nitinol (a shape memory alloy of nickel and titanium) wire with 5 helical loops ranging in diameter from 2.8 to 1.1mm at its tip.

To treat an ischemic stroke, the MERCI device is inserted into the femoral artery and fed through the vasculature to the site of the embolus where it ensnares the clot and completely removes the blockage from the patient's body. Briefly, the microcatheter delivers the retriever to the clot in its straight configuration before being withdrawn to deploy the coil. The BGC is a larger catheter (2.1mm diameter) with an inflatable balloon at its tip. Once the location of the clot is identified using angiography, the BGC is inserted through a small incision in the femoral artery in the groin and is maneuvered up to the carotid artery in the neck. Next, the microcatheter and a guide wire are deployed through the BGC and placed just beyond the clot. The physician then deploys the retriever device to engage and ensnare the clot. Once the clot is captured, the BGC is inflated to temporarily arrest forward flow while the clot is being withdrawn. The embolus is then pulled into the BGC and completely out of the body. The balloon is deflated, and blood flow is restored [91].

However, even in the case that the MERCI device successfully removes a clot from the patient's body, the ischemic penumbra may not survive. This is because reperfusion can cause cells in the ischemic penumbra to undergo delayed apoptosis due to the release of nitrous oxide and free-radicals as part of the ischemic cascade

[92]. After the MERCI device is deployed but before the embolus is removed, it is technically feasible to deliver pharmacologic neuroprotectants intraarterially to the ischemic territory through the microcatheter to mitigate the risks associated with recanalization. This is the concept of Intra-Arterial Selective Neuroprotection (IA-SNP).

Although many candidate neuroprotectant drugs exist [92], it is not possible to deliver them intra-arterially using the current standard small animal model for acute ischemic stroke. In this widely used model, the carotid artery of the animal is occluded using a thin filament that has a larger bulb on its distal tip. This bulb has to date been formed by melting the tip of a suture [93], or by coating the tip of a suture with silicone [94, 95]. This method of causing an infarct is minimally invasive, reversible, and effective. However, as it has no fluid delivery capabilities it is unable to accurately mimic the clinical possibility of selectively delivering neuroprotectants to the ischemic region preceding recanalization.

The goal of this project was to develop a novel small animal model of ischemic stroke which could reversibly arrest blood flow to the brain to cause an infarct, and also deliver candidate neuroprotectants intra-arterially to the ischemic tissue prior to the re-establishment of blood flow.

The design requirements of this small animal model are: (1) the catheter used to perfuse the ischemic region be small enough (170 – 200μm outer diameter) to pass through a constriction where the carotid artery enters the skull, and (2) the catheter must have side ports to deliver the prospective drugs. The main body of the novel IA-SNP microcatheter was constructed from commercially available polyimide tubing, and fluid delivery side ports were formed by laser micromachining. A catheter of this size is too small to cause a significant occlusion in the artery. To address this, we attached a bulb that is flexible enough to pass through the constriction while still being

large enough to simulate an embolus (350 – 450μm) to the distal tip of the catheter. We produced the flexible bulb from poly(dimethylsiloxane) (PDMS) because it has been widely characterized, its mechanical properties can be readily adjusted, and it can be cured into a wide range of shapes.

Extensive *in vivo* testing of these catheters showed that they could reproducibly cause reversible strokes in rats with no intracranial hemorrhage, and that they could also selectively inject fluid into different branches of the rat internal carotid artery (ICA). These results show that the novel catheters could become a valuable tool in preclinical testing of intra-arterial delivery of novel therapeutics for neurological disease including, but not limited to, ischemic stroke.

4.2 Materials and Methods

4.2.1 Microcatheter Fabrication

The stroke-inducing catheters were constructed from two parts: an occluding poly-dimethyl siloxane (PDMS) cylinder, and a polyimide fluid delivery catheter. A fabrication schematic is shown in Figure 4.1.

To form PDMS cylinders Sylgard 184 base and curing agent (Dow Corning) were mixed in a 10:1 weight ratio and degassed in a vacuum chamber. Approximately 2ml of this uncured PDMS was drawn into a 3ml luer-lock syringe attached to a 30G non-hypodermic needle. The PDMS was then injected into the lumen of a 5cm length of polyimide tubing (Small Parts Inc., Miramar FL). The tubing had an internal diameter that was the desired diameter of our occluding cylinder. After curing the PDMS in the tubing at 80°C for 2 hours, the PDMS cylinder was carefully removed

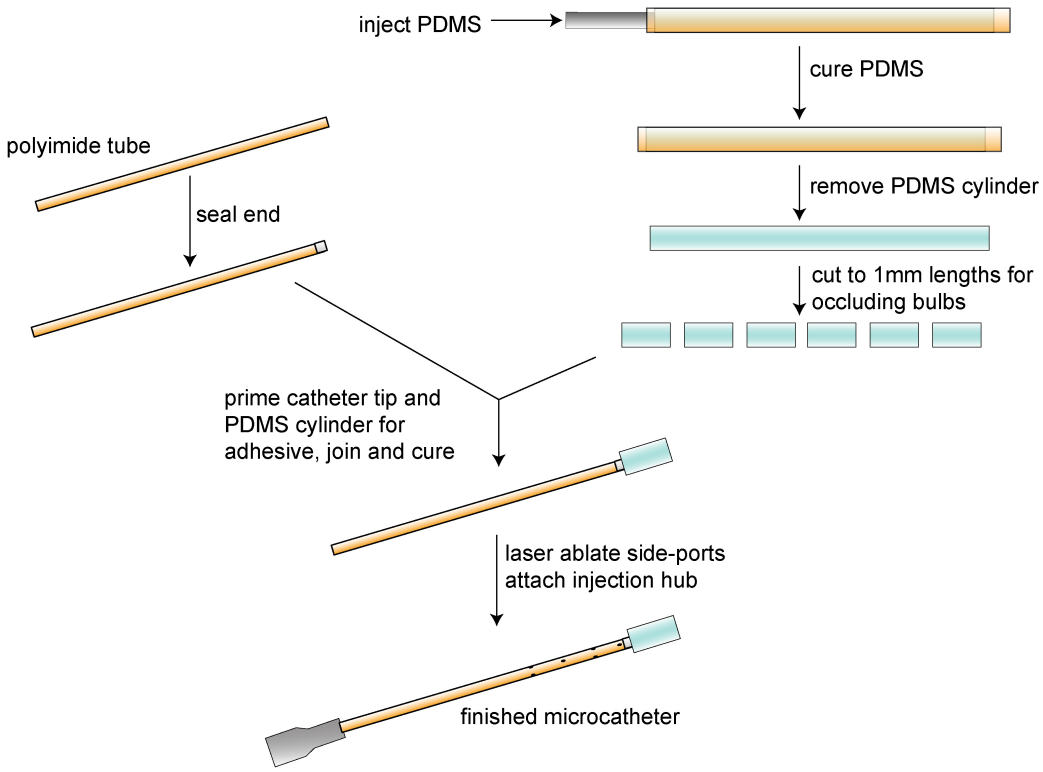

Figure 4.1. Schematic showing microcatheter fabrication procedure

from the tubing and cut into 1mm lengths using a razor blade and a specially designed cutting guide.

The PDMS cylinders were placed standing up on a clean glass microscope slide and were treated for 3 seconds each with a hand-held corona treater (model BD20-AC, Electo-Technic Products Inc., Chicago IL). This treatment cleaves the methyl groups from the surface of the PDMS, exposing the reactive siloxane backbone. Using a syringe with a 30G needle, a drop of Bondit™ A-3 primer (Reltek LLC, Santa Rosa CA) was applied to each cylinder and allowed to air-dry for 15 minutes.

Meanwhile, the fluid delivery microcatheter was prepared by blocking one end of a 15cm length of polyimide tubing (049-I, Microlumen Inc., Tampa FL) with a small amount of epoxy (Epoxy 907, Miller-Stephenson, Danbury CT). The epoxy was cured at 80°C for 1 hour. The blocked end was then placed on a glass slide and treated with a drop of Bondit™ A-3 primer and allowed to air dry for 15 minutes.

The PDMS cylinders were bonded to the blocked catheter tips using Bondit™ B45-TH epoxy (Reltek LLC, Santa Rosa CA). The catheter tips were dipped in mixed but uncured epoxy and were joined to the treated end of one of the PDMS cylinders under a stereoscope. The glued catheters were then placed upright in a specially designed frame in an oven at 100°C for 4 hours to cure the epoxy. If any of the cylinders slipped off the distal tip of a catheter during the cure, the tip was removed and the process was repeated.

Next, the fluid delivery side-ports in the distal end of the catheter assemblies were laser machined using an excimer laser (Maestro 1000, Resonetics Inc., Nashua NH). Four pairs of holes were machined through the catheter at 1mm intervals from the occluding bulb and each pair was rotated by 90 degrees. Finally, polypropylene injection hubs (Small Parts Inc., Miramar FL) were glued to the proximal ends of the

catheters with epoxy (Epoxy 907, Miller-Stephenson, Danbury CT), which was cured at 80°C for 1 hour.

Two types of microcatheter were produced. The first had no occluding PDMS bulb and was designated "μcath1". The second, designated "μcath2", had a 450μm diameter PDMS cylinder.

4.2.2 *In vivo* Catheterization Procedure

Sixteen adult male (270-330g) Sprague-Dawley rats were anesthetized using isofluorane gas (1-2% in 2 L O_2) delivered via facemask. An incision was made in the scalp, and a transcranial laser Doppler probe was secured to the skull 3mm posterior and 5mm lateral to bregma to monitor blood flow in the cortex as the catheterization was performed. Next, the animal was turned to the supine position, and a 24-gauge tail vein catheter was placed. In non-survival animals (#1-2), 3000u/kg intravenous heparin was given in 2mL normal saline (NS). In survival animals (#3-16), intravenous tobramycin (antibiotic) was administered (180mg/kg in NS). The right ICA was exposed via a midline neck incision, the occipital artery sacrificed, the pterygopalatine artery permanently ligated, and an arteriotomy made in the right external carotid artery (ECA) as described previously [96]. A microcatheter loaded with 7-0 polyimide suture was introduced into the cervical ICA and advanced 22-23mm (μcath1) or 18-20mm (μcath2) cephalad to the carotid bifurcation. With the catheter in place, a temporary ligature was placed around the cervical ICA. This surgical method and the imaging methods described below were reviewed and approved by the Weill-Cornell Medical College IACUC.

4.2.3 Angiographic and Perfusion Imaging

After placement of μcath1, thoracotomy was performed on animal #1 and the right atrium of the heart was sectioned. Gadolinium diethylenetriamine pentaacetic acid (Gd-DTPA, Magnevist, Wayne, NJ) diluted 1:1 with NS was injected via the ICA microcatheter (300μL over 10 minutes). The brain was removed, incubated in 10% neutral buffered formalin (Sigma-Aldrich, St. Louis, MO) for 30 minutes, and transferred to a custom made 1.7cm diameter receiver coil. *Ex vivo* magnetic resonance imaging (MRI) was then performed using three-dimensional magnetization prepared rapid gradient echo (MP-RAGE).

After placement of μcath1 animals #2-4 were transferred to the MR scanner where dynamic susceptibility contrast perfusion weighted imaging (DSC-MR) was performed before, during and after Gd-DTPA injection. Magnevist:saline (1:1) was delivered intracranially via manual injection with a 3mL syringe (Becton Dickinson) and a SmartPrep kit (TopSpins, Ann Arbor, MI) in series with μcath1. Magnevist:saline was injected over 20sec during dynamic gradient echo (GRE). After placement of μcath2, DSC-MR was performed on animals #5-7 using the same methods.

After placement of μcath2, animal #8 was transferred to a microPET focus 220 (CTI, Siemens, Malvern, PA). 20 μCi ^{18}F-labeled deoxyfluoroglucose (18FDG) in 10μL NS was injected via μcath2 over one minute. Five minutes later, a one-minute acquisition was performed. Five minutes later and with the animal in the same position, 412μCi in 206 μL was injected over 10sec via tail vein. Five minutes later, a second one-minute acquisition was performed. The animal was removed from the microPET system and transferred to the MR scanner, where axial T1-weighted images were acquired using a custom made 5cm diameter receiver coil. Animal #8 was

sacrificed immediately after MR acquisition. MicroPET images then were manually coregistered with raw axial T1 MR images and sagittal and coronal reformats according to the external contour of brain.

4.2.4 Evaluation of Iatrogenic Injury of Catheterization

Animals 9-16 were examined for catheterization related neurologic injury. In animals #9-12, μcath1 was advanced 22-23mm under continuous Doppler monitoring and 400 μL NS was injected over 20 min. In animals #13-16, μcath2 was advanced 18-20mm and 200 μL NS was injected over 20 min. In all eight animals, the ICA microcatheter was removed within 25 minutes of placement, pulsatile, anterograde flow was re-established in the cervical ICA and the neck incision closed. Forty-eight hours later, paw strength and the presence/absence of circular gait were tested. Animals were re-anesthetized and transferred to the MR scanner. T_2 weighted Fluid Attenuated Inversion Recovery (FLAIR) was performed using the previously described 5cm diameter solenoid receiver coil. Animals were sacrificed using intraperitoneal injection of high dose Nembutal (SleepAway^{TM}). Brains were removed, cut into 100μm sections and stained with 1% triphenyl tetrachloride (TTC, Sigma), as previously described [97].

4.3 Results

4.3.1 Microcatheter fabrication

The finished microcatheters were constructed from two parts, a 15cm length of polyimide tubing and a PDMS cylinder that was attached to the distal end of the

polyimide tube (Figure 4.2). The polyimide tube had and external diameter of 169µm and had four pairs of laser machined side-ports to allow for fluid delivery. The side ports were 35µm in diameter, and each pair was spaced 1mm apart and rotated by 90° from the last. The PDMS cylinder was 1mm long and 450µm in diameter, and served to occlude the ICA terminus and its branches. The join between the PDMS cylinder and the end of the polyimide tubing was examined under both tension and torsion, and in all cases the PDMS cylinder ruptured before the adhesive join. This suggested that the bulbs would stay attached to the catheter during the catheterization procedures.

4.3.2 *In Vivo* Microcatheter Characterization

To characterize the microcatheters *in vivo*, 16 Sprague-Dawley rats were catheterized and fluid was injected intra-arterially via one of the two microcatheters. The territories of µcath1 and µcath2 injection were examined using magnetic resonance imaging (MRI). MRI, a non-invasive imaging technique, uses the interactions between the nuclei of atoms in a sample and external magnetic fields and radio waves to generate high quality images. Briefly, when the nuclei of atoms that have net spin (e.g. hydrogen nuclei) are placed in an external magnetic field, they line up along, and precess around the axis of the magnetic field at a specific frequency, known as the Larmor frequency. If a radio-frequency (RF) pulse at the Larmor frequency is applied to the sample, the nuclei can be flipped from being aligned with the external field to being aligned perpendicular to it. After the RF pulse is switched off the nuclei relax to their equilibrium state, and emit a radio-frequency free induction decay signal (FID). This signal forms the basis of the final image. By applying particular patterns of RF pulses and magnetic field gradients to the sample different features can be highlighted or suppressed in the final image.

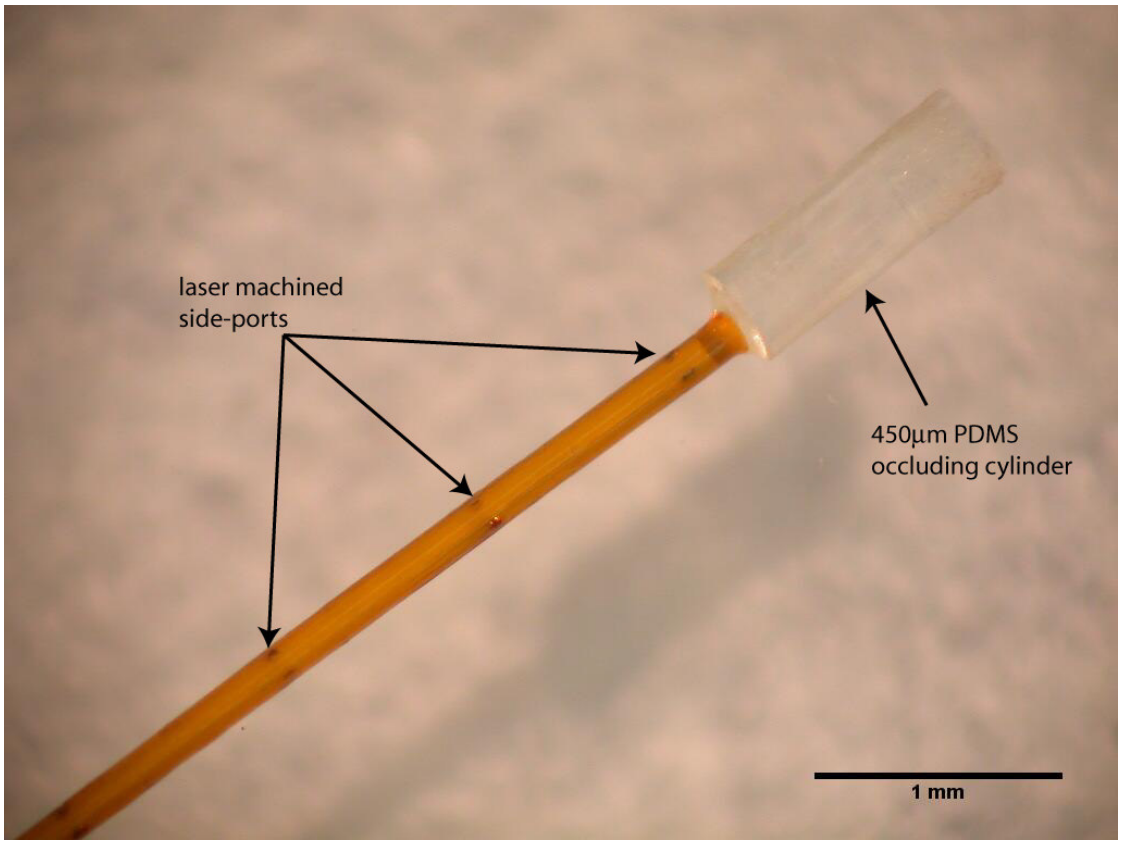

Figure 4.2. Photograph showing microcatheter with attached 450µm PDMS cylinder. Note four pairs of side ports spaced 1mm apart.

To validate the injected territory of μcath1, DSC-MR was acquired through a single axial plane in the rat forebrain 2mm posterior to bregma during and after Gd-DTPA injection. Due to concentration effects, Gd-DTPA appears dark on this susceptibility-sensitive sequence. Injection via μcath1 during imaging demonstrated gadolinium perfusion of the right cerebral hemisphere (Figure 4.3) with sparing of the left. During the initial phases of injection via μcath1, the hypothalamus opacified in the same early phase as the rest of the hemisphere but washed out more slowly.

A 450μm PDMS cylinder was affixed to the distal tip of μcath2 to occlude the ICA terminus and its branches, allowing selective injection of ipsilateral forebrain structures with sparing of cortex. The territory of injection of μcath2 was examined by performing perfusion MRI before, during, and after the injection of Gd-DTPA (a paramagnetic contrast agent) through the catheter while it was in position in the ICA. The results are shown in Figure 4.4. Due to concentration effects, Gd-DTPA again appears dark in these susceptibility-sensitive images. The different panels of the sequence demonstrate early and late arterial phases (A, B respectively), and early and late venous phases (C, D respectively) of the perfusion imaging opacification.

^{18}FDG injected through μcath2 perfused an ellipsoid region of the ventral forebrain (Figure 4.5). Using ear canal susceptibility effect as a landmark (Figure 4.5, panel D), the position of each axial image relative to bregma was determined for anatomic correlation [98]. The volume of rat brain occupied by >195μCi/mL was approximately 180μL, centered in the region of the hypothalamus (-1.3mm to -4.5mm relative to bregma) and tuber cinerum (-1.8 to -3.3). Of note, no activity was seen in the anterior choroidal territory (lateral thalamus), or substantia nigra (-6.3 to -4.8), which is supplied predominantly by the posterior circulation.

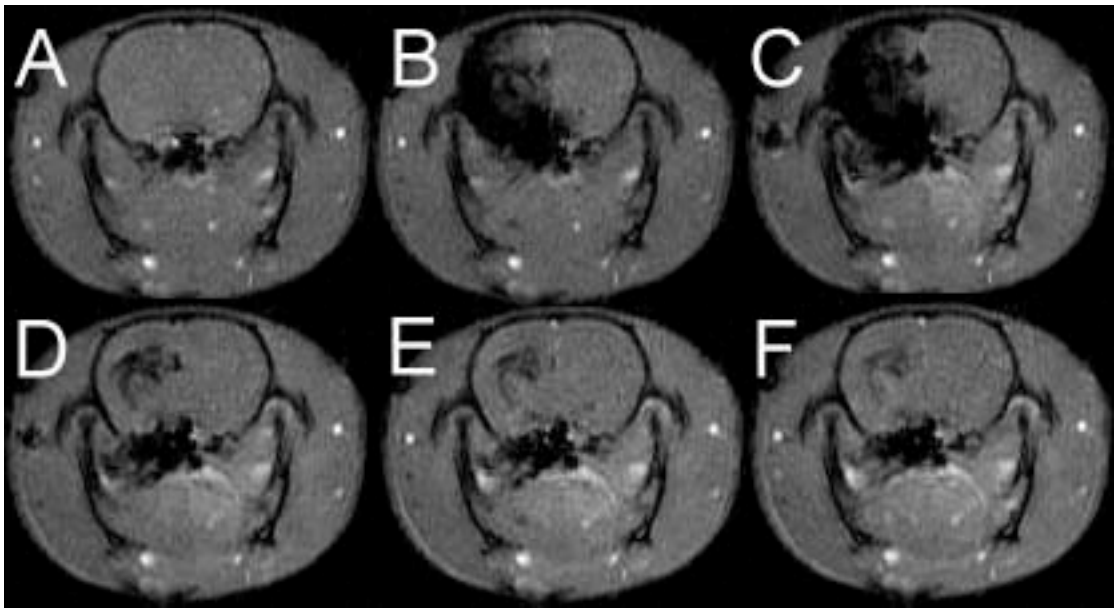

Figure 4.3. Injection of gadolinium into a single cerebral hemisphere. Approximately 50-100μL of 1:1 Magnevist:NS was hand-injected via μcath1 over 20 sec. Axial T1 GRE-MR images were acquired 4-5mm caudal to bregma at 0.0 (A), 11.2 (B), 22.4 (C), 44.8 (D), 56.0 (E) and 112 sec (F) after gadolinium injection.

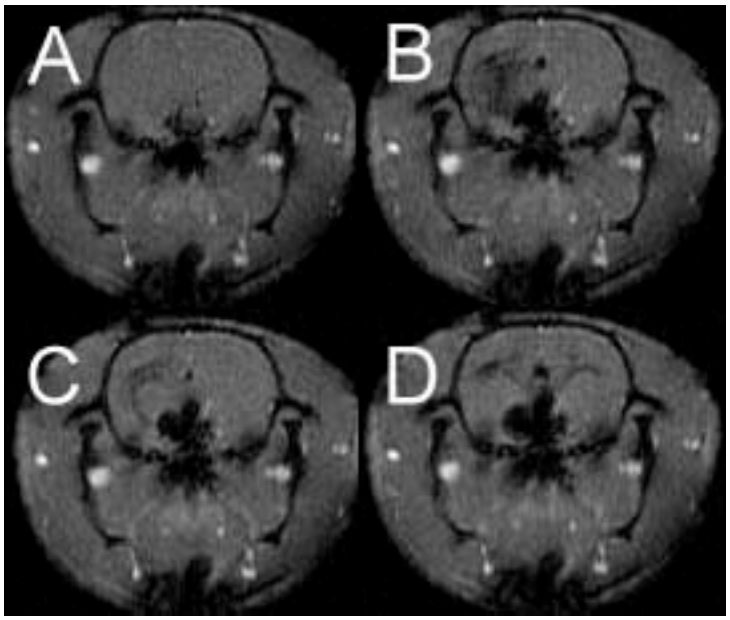

Figure 4.4. Time course of axial T_1 GRE-MR images acquired 4-5mm caudal to bregma taken during a 20sec hand-injection of Magnevist:NS via μcath2. Images were acquired at 5.6 (A), 22.4 (B), 44.8 (C) and 56.0 sec (D) after the beginning of injection. (A) and (B) represent early and late arterial phases, respectively. (C) and (D) represent early and late venous phases.

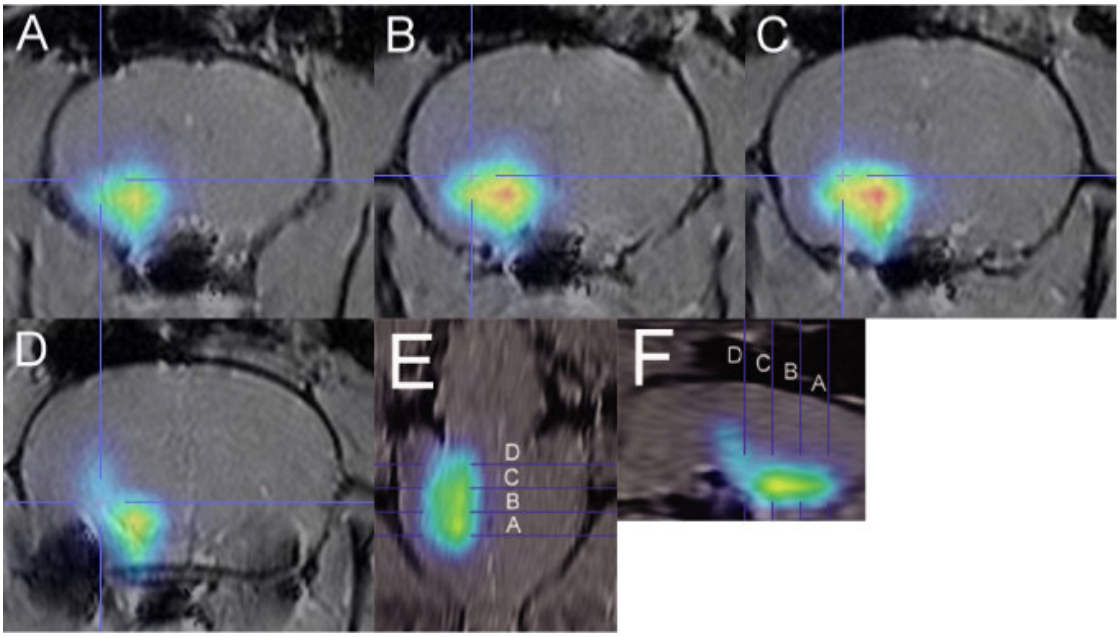

Figure 4.5. Selective injection of ^{18}FDG into hypothalamus. MicroPET data was acquired five minutes following injection of 20µCi ^{18}FDG in 10µL NS via µcath2 over one minute. Activity is represented by red (270µCi/mL), yellow (240µCi/mL), green (195µCi/mL) and blue (90µCi/mL). Manual co-registration was performed with 2mm thick axial T1-weighted images and with coronal and sagittal reformats. Panel A is 1.0-0.8mm rostral to bregma, panels B-D are 1.0-1.2mm, 3.0-3.2mm 5.0-5.2 mm caudal to bregma, respectively.

4.3.3 Evaluation of Iatrogenic Injury of Catheterization

Four animals were catheterized with μcath1 for 25 minutes, and monitored for changes in blood flow within the MCA territory. A transient flow reduction of 5-15% (monitored via Doppler probe) was observed for 2/4 animals. In both cases, the slight flow abnormality was first detected just as μcath1 crossed the skull base. In both animals, this small abnormality abated within five minutes. Four more animals were similarly examined using μcath2. 4/4 demonstrated a 40-73% reduction in flow within the MCA territory. In all four, the Doppler abnormality persisted until μcath2 was removed and the ICA revascularized. Figure 4.6 is a Doppler probe trace showing the effect of a catheterization with μcath2 on cortical blood flow. As the PDMS bulb of the catheter occludes the middle cerebral artery (MCA) the blood flow to the cortex drops to between 40% and 50% of baseline, indicating that the catheters are capable of simulating the effects of an embolus in the MCA. Forty-eight hours after microcatheter removal, no motor or visual field defect was detected on examination of these eight animals. There was no T2-bright lesion or extra-osseous region of susceptibility effect on MR examination. There was no intracranial hemorrhage on necropsy and no triphenyl tetrachloride lesion on histology to suggest infarction.

4.4 Discussion

The microcatheters were constructed from 169μm outer diameter polyimide tubing, with 25μm thick walls. Although larger polyimide tubing provides easier device

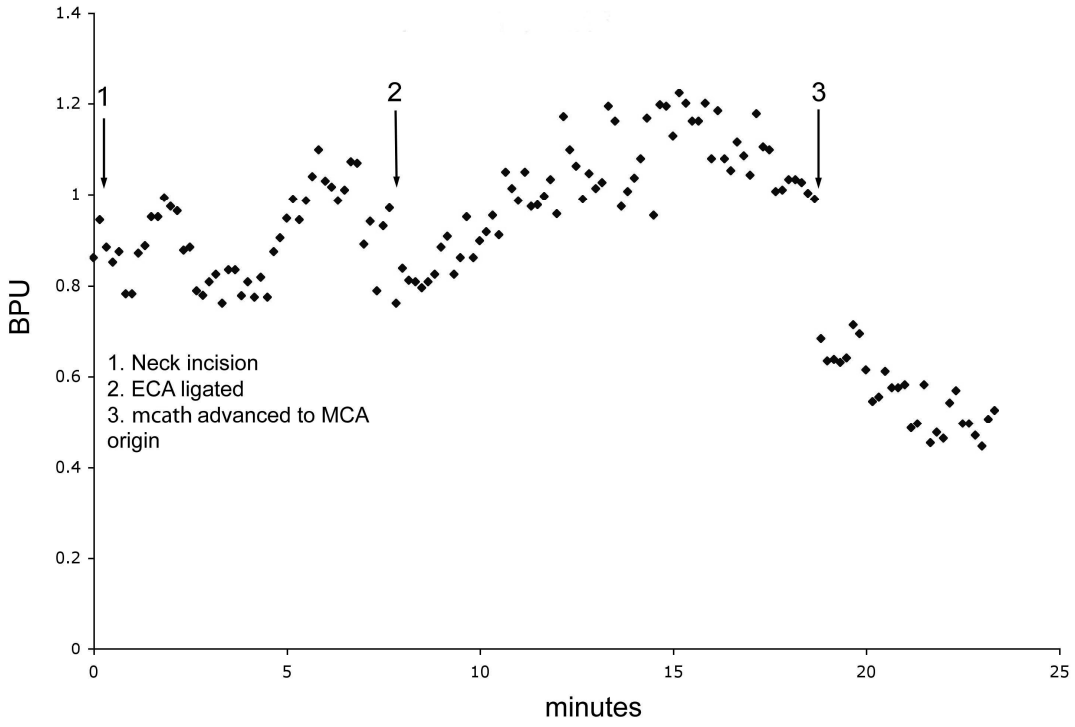

Figure 4.6. Doppler probe trace showing cortical blood flow in the middle cerebral artery (MCA) territory during MCA occlusion. The x-axis depicts time from an initial neck incision (t=0). The y-axis demonstrates cerebral blood flow in arbitrary units (blood perfusion units) within a 1-2mm^3 volume of forebrain cortex measured by a laser Doppler probe embedded in the parietal bone. When the microcatheter is advanced to the MCA origin, cortical blood flow drops to 40-50% of baseline.

assembly, it was found to be too rigid to navigate the arteries of the neck and head of the rat without rupturing the fragile blood vessel walls. The polyimide tubing used in the final microcatheter was the smallest tubing in which we could reproducibly machine sufficiently large side-ports without failure of the catheter, and it was consistently able to be passed into the ICA without damaging the vessels.

The occluding bulb was fabricated from a PDMS cylinder. The cylinder was used as it provided more contact area between the bulb and the vessel wall compared with other geometries (e.g. a sphere). Furthermore, the use of a cylindrical bulb required that the PDMS be molded in the lumen of a piece of tubing of the desired final diameter. As a result, the final diameter of the occluding PDMS cylinders was highly reproducible and uniform.

The microcatheters could consistently inject specific territories of the brain with minimal contralateral leakage. μcath1 was able to inject the entire cerebral hemisphere through the anterior cerebral and middle cerebral arteries (ACA and MCA, respectively). The large occluding bulb of μcath2 prevented the injected fluid from passing into the ACA or MCA (Figure 4.7). In this case the catheter injected the anterior choroidal (AChA) and hypothalamic arteries (HTA) perfusing the hypothalamus and lateral thalamus without affecting the cortex. In the animal injected with ^{18}FDG, fluid was seen in the hypothalamus but not in the territory of the AChA, however in the perfusion MR images fluid was observed in the AChA. Reconciling these findings hinges on the technical considerations. Acquisition of microPET images shown in Figure 4.5 was started five minutes after tracer injection. Given the rapid washout of the lateral thalamus visualized in Figure 4.4, it is not surprising that activity was absent in the lateral thalamus during delayed microPET image acquisition.

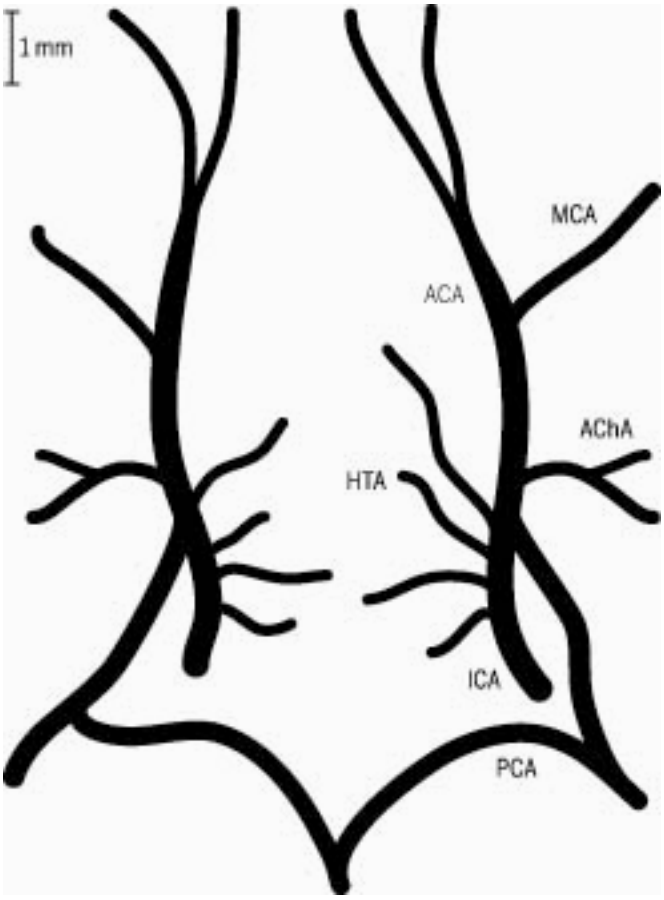

Figure 4.7. Intracranial arterial supply in rat with rostral oriented upward. Anterior (ACA), middle (MCA) and posterior (PCA) cerebral and hypothalamic (HTAs) and anterior choroidal (AChA) arteries are labeled (adapted from [99]).

These data illustrate that the use of two catheters with different distal geometries (bulb and no bulb) allow for the injection of different territories of the rat brain. This could be a major advantage of this technique in pre-clinical trials of intra-arterial delivery of drugs for neurological disorders as it provides a new level of control over the specific areas of the brain that receive the therapy.

An important factor that must be evaluated before this system could be used to examine intra-arterial delivery of novel therapeutics in potentially valuable rodent models is the safety and neurological effect of the catheterization and injection procedure. Transcranial Doppler monitoring of the cortical blood flow during the catheterization showed that μcath1 (no distal bulb) had little to no effect on the blood flow in the MCA territory, and that any effect resolved itself within a few minutes. μcath2 (450μm PDMS cylinder) had a significant effect on the blood supplied to the ipsilateral MCA territory, and flow changes of 40-70% of baseline were observed. This reduced flow persisted until the microcatheter was removed from the ICA. Despite this, neither catheter was observed to cause any long term neurological deficit if left in place for up to 25 minutes.

4.5 Conclusions

These novel microcatheters permit the selective intra-arterial injection of specific regions of the rat brain. These devices hold promise for intra-arterial delivery of novel therapeutic agents, including but not limited to pharmacotherapy, viral vectors, nucleotide probes, radiolabeled ligands, nanoparticles or stem cells in rat models for neurological disease. Furthermore, if used in conjunction with the imaging techniques described above, valuable information about the real-time distribution of the injected drugs can be obtained.

These catheters are capable of simulating an embolus, but to date the side-ports have not remained open long enough to allow for injection of potential neuroprotectants prior to recanalization due to clotting around the distal tip of the catheter. The next generation of catheters will attempt to overcome this issue by immobilizing an anti-clotting agent (e.g. heparin) on the surface of the catheters.

Future work on this system will involve more thorough characterization of the distributions and territories of the brain injected as a function of different injection parameters such as flowrate, and volume of delivery.

CHAPTER 5

CONCLUSIONS AND FUTURE WORK

This dissertation addresses some of the issues associated with neural drug delivery through three main investigative routes: development of new and more effective delivery devices, comprehension of drug transport mechanisms, and improvement in pre-clinical testing models for new therapeutics. Although this work does not fully resolve these issues, it provides a solid foundation for future research in these areas. This final chapter will summarize the findings presented in previous chapters, and discuss some of the potential work that could build on these results.

The design, fabrication and characterization of a novel, flexible microfluidic device for chronic CED applications were described in chapter 2. The flexible device was made from parylene, and was supported during insertions by a biodegradable PLGA scaffold which is designed to erode over time to leave only the parylene probe in the tissue. The microfluidic system was able to penetrate murine neural tissue, and effectively deliver fluid to the brain in a controlled way during acute infusions. The flexible nature of the device reduces the mechanical mismatch between the tissue and the implant, which should provide improved long term biocompatibility, and increase the effectiveness of therapeutics delivered using this system.

To date, this microfluidic system has been tested in acute implants in a mouse model, and although this is a critical first step in developing a chronic infusion device the next goal should be to examine the performance of the probe in chronic experiments. The chronic studies should examine the fluidic performance of the flexible probe compared to standard small gauge needles and silicon based

microfluidic devices. The studies should also examine the tissue response to the implants to evaluate whether the flexible device decreases glial scar formation and microtearing at the tissue-implant interface. It would also be valuable to examine whether using the PLGA scaffold to deliver an encapsulated drug (e.g. an anti-inflammatory) as it degrades can positively affect the chronic performance of the system, as this is an advantageous capability which other systems do not provide. Finally, efforts to scale up this system should be undertaken, as the 3mm implantable length is not big enough to reach deep grey matter structures in rats, rabbits, etc.

Although this system was conceived as a chronic fluidic implant for CED, the use of an external biodegradable scaffold could be of tremendous interest to researchers wishing to perform long term electrical recording in deep structures of the central nervous system, as it allows for implants to be inserted several millimeters into tissue. Previous flexible microfabricated electrodes have been shown to penetrate only into the cortex, not to deeper structures [55, 100-102].

Understanding the manner in which large drugs are transported through the brain during CED is of critical importance to designing protocols that will improve the spatial control of drug distributions, and minimize drug associated side-effects. Chapter 3 described the use of 2-photon excited fluorescence (2PEF) microscopy to study the motion of large particles through the brain during delivery via CED. We observed that perivascular spaces provide high permeability conduits for transport of large constructs (greater than approximately 50nm diameter). Furthermore, we saw that perivascular transport is size dependant. We showed that for smaller particles that can pass through the ECM, the fraction of the infused particles that move through the perivascular spaces rather than the ECS is lower than for large particles that undergo significantly hindered transport through the ECM. These results suggest that perivascular transport can have a significant effect on the fate of infused compounds,

and that the vasculature of the target area should be considered before performing CED to reduce unwanted drug distributions.

Further experiments need to be carried out to fully characterize the effect of how exclusion from the ECM promotes perivascular transport. This could be done by infusing a small fluorescent tracer that does not undergo hindered transport through the ECM while monitoring the distribution using 2PEF, and evaluating the fraction of the infused dye that localizes in the perivascular spaces. This might elucidate a cut-off hydrodynamic diameter of infusate where transport in perivascular spaces becomes significant. It would also be interesting to increase the porosity of the extracellular matrix through enzymatic degradation or osmolitic swelling to see if this could decrease perivascular transport of large particles in cases where this would be undesirable.

Chapter 4 outlined the fabrication and characterization a novel endovascular microcatheter for use in small animal models of selective intra-arterial neuroprotection. The microcatheter was made from 169μm polyimide tubing that had microfluidic side-ports laser machined in the end of the poyimide tubing for fluid delivery. Some catheters had a PDMS bulb attached to the distal tip to arrest blood flow in the artery. By using these different catheter designs (with and without distal bulbs), different areas of the rat brain could be unilaterally injected (whole hemisphere with no bulb, only deep brain structures with bulbed catheters). These devices hold promise for intra-arterial delivery of novel therapeutic agents, including but not limited to pharmacotherapy, viral vectors, nucleotide probes, radiolabeled ligands, nanoparticles or stem cells in rat models for neurological disease.

These catheters are capable of simulating an embolus, but to date the side-ports have not remained open long enough to allow for injection of potential neuroprotectants prior to recanalization due to clotting around the distal tip of the

catheter. It may be possible to overcome this problem by immobilizing an anti-clotting agent, such as heparin, on the surface of the device to keep the fluidic ports open during the multiple hour occlusions required to accurately simulate stroke conditions.

Future work on this system should involve more thorough characterization of the distributions and territories of the brain injected as a function of different injection parameters such as flow rate, and volume of delivery.

APPENDIX I

DETAILED PARYLENE PROBE AND PLGA SCAFFOLD FABRICATION PROCEDURE

The complete flexible implantable microfluidic device consists of two parts: a flexible parylene microfluidic component, and a rigid biodegradable PLGA scaffold. The scaffold supports the parylene device during insertion and degrades over time to leave just the parylene microfluidic device. The parylene microfluidic probe is produced using standard top-down microfabrication techniques, and the PLGA scaffold is formed by microembossing PLGA in a PDMS mold. This appendix will give an in depth description of the fabrication steps for each part of the device, and detail how to prepare the completed device for use.

I. Parylene Microfabrication

1. The first step in the fabrication procedure is to prepare the silicon wafers for the base layer of parylene. It's best to work with batches of three wafers (100mm diameter, single side polished) for the process as this is the maximum capacity of many of the etching and deposition tools used. To clean the wafers of any organic residues, place them in the 70°C nanostrip bath for 15 mins, and wash them in the dump-rinse tank. Then dry the wafers in a spin-rinse drier. Finally, dehydrate the wafers on a 175°C hotplate for 3mins each.
2. Next, etch the wafers in the PT-72 with a CF_4 plasma for 1min to roughen the surface. Use program 8 at a power of 150W.

3. Place the wafers on glass microscope slides on the platen of the parylene deposition tool (CNF or NBTC). Raising the wafers off the platen ensures that the parylene coating wraps underneath the wafers. Also place Si wafer chips at the center, middle, and edge of the platen to determine the thickness of the parylene film. Deposit approximately 5g of parylene. After the deposition check the parylene thickness by slicing the film on the Si chips with a razor blade and measuring the layer on the P-10 profilimeter.
4. Roughen the surface of the parylene layer with a 30s, 100W O_2 plasma in the Glenn.
5. Place the wafers in a spin-coater and spin P-20 at 4000rpm. Next spin Shipley 1045 at 500 rev/s (5s, 1000 rev/s ramp), 800 rev/s (5s, 1000 rev/s ramp), and 1000 rev/s (45s, 1000 rev/s ramp) using a dynamic pour. Soft bake the resist at 90°C for 3mins on a hot plate.
6. Expose the wafers on the EV-620 using the channel mask at a dose of ~250mJ/cm^2. Develop in 300 MIF using a double-puddle technique, and hardbake the wafers at 90°C for 1min.
7. Measure the resist profiles using the P-10 profilimeter. This recipe should give a channel height of approximately 10.7μm.
8. Descum the wafers with another 30s, 100W O_2 plasma in the Glenn, before depositing a second 5g film of parylene (as before).
9. Roughen the surface of the parylene with another 30s, 100W O_2 plasma in the Glenn before depositing 150nm of conformal Al using the NBTC evaporator. The conformal application ensures Al coverage of the sidewalls of the channels.
10 Spin P-20 as before on the Al coated wafers. Then spin 1045 at 500

rev/s (5s, 750 rev/s ramp), 800 rev/s (5s, 750 rev/s ramp), and 1400 rev/s (45s, 1000 rev/s ramp) using a dynamic pour. Softbake the wafers for 3min at 90°C .

11. Expose the wafers on the EV-620 using the probe body mask at a dose of ~250mJ/cm^2. Develop in 300 MIF using a double-puddle technique, and hardbake the wafers at 90°C for 1min.
12. Etch the exposed Al in aluminum etch until visibly gone, plus 1min more.
13. Etch the exposed parylene in an O_2 plasma in the Oxford 81 (O_2 Clean recipe, 150W) until the wafer is etched to the bare Si. Note: this step can take over 2hrs.
14. If there is any photoresist remaining on the wafer strip it with acetone before stripping the remaining Al mask in aluminum etch. This etch will take longer than before as the Al has been thoroughly oxidized by the plasma.
15. The final step is to clear the photoresist from the channels. It's best to only clear the wafers as you need them. Place a wafer in a 6" evaporating dish with enough acetone to cover the wafer to a depth of ~3mm, and cover. Leave the wafer for ~12hours. Once the channels are clear thoroughly rinse the wafer with IPA, and DI water.

II. PLGA Microfabrication

1. To produce the Si master for the hot-embossing procedure clean a 100mm single side polished Si wafer as described above.
2. Spin P-20 at 4000 rev/s for 40s, before spinning 1045 at 400 rev/s (5s,

750 rev/s ramp), 800 rev/s (5s, 750 rev/s ramp), and 1400 rev/s (45s, 1000 rev/s ramp) using a dynamic pour. Soft bake the wafer at 90°C for 3min.

3. Expose the wafers on the EV-620 using the probe body mask at a dose of ~250mJ/cm^2. Develop in 300 MIF using a double-puddle technique, and hardbake the wafers at 90°C for 1min.
4. Clean the native oxide from the wafers with a 1min bath in 30:1 BOE. This step is crucial to avoid forming silicon grass during the Bosch Etch.
5. Descum the wafer with a 30s, 100W O_2 plasma in the Glenn before the deep silicon etch.
6. Etch the wafer using the Bosch etcher (Unaxis) and the '1thru' recipe. It takes roughly 550 or 600 loops to etch 200μm of Si using this recipe and mask, but regularly stop the etch to measure the actual depth of the etch.
7. Strip the photoresist from the wafer, and place the wafer under vacuum with a drop of tridecaflouro-1,1,2,2 tetrahydroctyl trichlorosilane on a glass slide for 2-3 hours to silanize the wafer. If this step is skipped the PDMS will covalently bond with the wafer while curing and ruin the master.
8. The mix approximately 55g of PDMS (10:1 base:curing agent by weight), and de-gas the mixture thoroughly until no large bubbles can be seen (usually 5-10 pump-down/vent steps). Tape the Si master into the bottom of a 150mm plastic petri dish (PDMS will bond to glass), and pour the uncured PDMS over it. De-gas the the wafer/PDMS again until no bubbles can be seen on the features of the Si master. Use shims

to level the petri dish and leave the PDMS overnight to cure partially. Once the PDMS is partially cured, place it in a 70°C oven for 2hrs to fully cure.

9. Repeat this step using just a petri dish (no wafer) to form the unpatterned top of the mold.
10. After the PDMS is cured, peel it from the petri dishes and cut it into appropriately sized squares (~1") using a razor blade. If you try to do this while the PDMS is on the wafer in the dish you run the risk of cracking and ruining the master.
11. Place a few granules of the PLGA you want to use in the outlines of the scaffolds in the mold bottom. You only need enough to fill the space of the mold, and it's important to not use too much. Unfortunately, trial and error is the only way to determine the optimum amount of PLGA to add.
12. Carefully place the unpatterned piece of PDMS on top and sandwich the assembly between two small squares of aluminum plate. Place this sandwich on the platen of the hydraulic press.
13. Lightly close the platens of the press on the sandwich, and heat the assembly to above the glass transition temperature of the PLGA (this temperature will depend on the PLGA used).
14. Press the sandwich using the fine-control mode of the press to a pressure of ~90psi, and press for at least 10mins.
15. Cool the assembly back to room temperature by circulating cold water through the platens. Make sure to regularly check for ballooning or failure of the water supply tubing as the thermal cycling can damage the tubing. Also make sure that the platens are thoroughly cooled (i.e.

cold to the touch) before releasing the pressure on the PDMS mold.

16. Remove the mold, and carefully disassemble it. The PGLA scaffolds can now be removed using fine tweezers and some very gentle flexing of the mold, or with a piece of double-sided adhesive tape affixed to a flat surface such as a spatula tip. The scaffolds can be removed from the tape by rinsing them with IPA.

III. Device Assembly and Use

1. Glue a 7.5cm length of PEEK tubing (360µm OD, 150µm ID, Upchurch Scientific) into the lumen of a 580µm ID, 1mm OD borosilicate micropipette (World Precision Instruments Inc.) using Miller Stephenson 907 epoxy. Prepare the epoxy by mixing part A and part B in a 1:1 volume ratio (by eye) and stirring well. The finished epoxy should be a pale blue color. The PEEK tube should extend for no more than 2-3mm inside the lumen of the pipette. Leave the epoxy to cure overnight.
2. To remove the parylene devices from the wafer, place a drop of IPA on the device you wish to remove. With the corner of a razor blade gently lift the body of the probe from the wafer. It's best to work slowly, and hold the blade at a very shallow angle. Slide the corner of the blade under the corner of the handling tab and work along the length of the probe body gently lifting the device from the wafer. The IPA should help to smooth the process, and if all goes well the device should float off the wafer in the IPA.
3. Next, use fine forceps and a stereoscope to remove the four tabs of the

fluidic channels that extend from the channel openings.

4. Insert one shank of the parylene device into the open end of the PEEK tubing under stereo-magnification. Use an anti-static gun to eliminate static charges on the tubing and device.
5. Use a small sliver of plastic or wood to apply a very small amount Miller Stephenson 907 epoxy to glue the device in the tubing. Use the bare minimum amount of epoxy required to get a complete seal around the device. Use an anti-static gun if it becomes difficult to cleanly apply the epoxy to the join.
6. Use a 1ml pipette tip inside a pipette-tip box to hold the glass micropipette upright while the epoxy cures. Cure the epoxy in an 80°C oven for 1-2 hours.
7. Connect the finished devices to the programmable pressure injector using a 1mm electrode holder. Test the devices by passing air through them while the tip is submerged in water. Bubbles mean that the channels are patent.
8. To prime the devices, connect them to the small vacuum pump using a microelectrode holder and some Teflon tubing. Submerge the entire parylene probe in the solution to be used, and back-fill the PEEK tubing and ~5mm of the glass micropipette by drawing a vacuum.
9. After the PEEK tubing has been filled use a 1ml syringe with a 28G microfil tip to fill the rest of the glass pipette from the open end. Be careful not to introduce bubbles to the lumen of the pipette.
10. To attach the microfluidic device to the insertion scaffold apply a small drop (~15µl) of 5-min epoxy (Devcon, Danvers MA) to the body of the scaffold, and carefully lay the primed microfluidic device on top under

a stereoscope. The epoxy couples the body of the scaffold to the body of the parylene device, leaving the shanks aligned but not connected. The shanks can be sealed together by briefly (<0.5s) dipping them in dichloromethane. This treatment removes the highly permeable fluidic track between the two parts of the system. Allow the assembly to air dry for at least 15 min to ensure that all residual dichloromethane has evaporated.

11. Next, use double-sided adhesive tape to attach the body of the scaffold/probe assembly to a custom made Delran block which can be mounted on a micromanipulator. This is the final arrangement used for inserting the device into tissue or gels.

APPENDIX II

DETAILED ENDOVASCULAR MICROCATHETER FABRICATION PROCEDURE

I. PDMS Cylinder Preparation

1. Prepare approximately 2g of PDMS (Sylgard 184) by mixing base and curing agent in a 10:1 weight ratio. Mix them in a disposable dish and use plenty of paper towels to wipe down everything to avoid getting PDMS everywhere. Degas the PDMS in a vacuum chamber to eliminate any large air bubbles.
2. Draw the PDMS into a 3cc syringe with a luer lock. Pour a small amount of PDMS into the hub of a 30G needle (non-hypodermic, Smallparts Inc.) to prime the hub. Affix the needle to the syringe making sure to eliminate any air bubbles between the hub and the needle.
3. Cut polyimide (PI) tubing with the same internal diameter as the desired external diameter of the PDMS cylinders to approximately 5cm lengths. Inject the uncured PDMS from the syringe into the PI tubing, leaving approximately 3-5mm of air space at each end of the tube.
4. Put the PI tubes in the oven at 80°C for 2 hours to cure the PDMS. Cut the PI tubes containing PDMS in half. Carefully split the ends of the PI tube with the air space using a razor blade. Peel away the split PI tubing using forceps to expose the PDMS inside. It's best to use the stereoscope for this stage, and be careful not to kink the PI tubing while

you dissect it. Once 1-2mm of the PDMS is exposed, grab it with a forceps and gently pull it from the PI tube. You need to be careful to pull the PDMS without twisting or bending it too much. Also, it's best not to try to extract the PDMS in one go; it helps to release the tension on the PDMS so that the interface between the PDMS and the PI tube can relax, and then reapply tension. If you do this stage carefully, it should be possible to remove intact PDMS cylinders from the PI tubing.

5. Examine the PDMS cylinder under the stereoscope, and cut away the end that was used for pulling it from the PI tube. Next, affix the PDMS cylinder to the cutting guide using double sided tape. Be careful to align the cylinder perpendicularly to the cutting guide; use the anti-static gun if static charges make the PDMS jump around. Use the sliding guide and a razor blade to cut the cylinder into 1mm lengths. Cut ~15% more cylinders than catheters you hope to make to account for losses in the rest of the fabrication steps.
6. Using extra fine tipped forceps, place the PDMS cylinders standing on their edges on a clean glass slide, distributing them evenly over the area of the slide. Plasma-clean the top surface of the cylinders using the handheld corona treater (Electro-Technic Products, Inc.). Use the straight wire electrode, and hold the tip ~5mm above the surface of the cylinder for 2 seconds. If you plasma treat the cylinders for any longer, the PDMS will be damaged and weakened.

II. Polyimide Catheter Preparation

1. Cut 12” pieces of PI tubing (from MicroLumen) into 6” lengths. Ensure that the cut is perpendicular to the axial length of the tubing.
2. Prepare Miller Stephenson 907 epoxy by mixing part A and part B in a 1:1 volume ratio (by eye) and stirring well. The finished epoxy should be a pale blue color.
3. Barely touch the original factory-cut end of the 6” section of PI tubing into the epoxy, just barely cover the end of the catheter. Wipe the excess epoxy from the tube with a kimwipe. Inspect the end of the tube to ensure that it is blocked. The ideal thickness of blockage is between 1 and 1.5 times the ID of the catheter.
4. Place the blocked catheters into glass capillaries, inside 1ml pipette tips, in a pipette tip box. This keeps the catheters straight and upright while they cure.
5. Cure the epoxy in an oven at 80°C for 1 hour.

III. Gluing - this step must be carried out immediately after plasma treatment of the PDMS cylinders

1. Affix a 30G non-hypodermic needle to the 5ml syringe of Bondit™ A-3 primer. This is available as a special order from McMaster-Carr, with a lead-time of 4-6 weeks.
2. Dispense 1 small drop of primer onto the primed surface of the PDMS cylinders. Make sure that the cylinders stay upright during this process so that you know which end has been treated. Allow the primer to air

dry for 15 minutes.

3. Lay the catheters so that the blocked distal ends lay on glass slides, and again apply a small drop of primer to each catheter tip, and allow the primer to air dry for 15 minutes.
4. Next, prepare the epoxy for the gluing. Place the cartridge of Bondit™ B45-TH epoxy in the dispensing gun, and affix the 2:1 plunger. Squeeze out a small amount of epoxy (~3cm disc) and mix well.
5. Once the primer has dried, barely dip the distal tip of the catheter into the epoxy and examine the coverage under the stereoscope. If you apply too little epoxy the PDMS bulbs will fall off, and if you apply too much epoxy surface tension effects will drag the cylinders off the catheter tips during the curing process. A good guideline is to see a small hemisphere of epoxy on the catheter tip with no epoxy on the sidewalls of the catheter.
6. While holding the catheter with epoxy in one pair of forceps, pick up a PDMS cylinder from the glass slide using some extra fine forceps. Make sure to keep track of which end has been treated, and align that end with the distal tip of the catheter. Lightly touch the two ends together, and the PDMS cylinder should stick to the catheter tip. If all has gone well, and your hands are steady, the two pieces should form a straight line. If the PDMS cylinder is askew, gentle nudges with a forceps can sometimes straighten it. However, it is occasionally necessary to repeat the gluing step with a new cylinder.
7. Once you are satisfied with the alignment of the PDMS cylinder carefully place the catheter in the capillary/pipette tip holder, and repeat for the rest of the batch. Do a final inspection of the catheter tips to

make sure none have slipped off, and carefully place the catheters in the oven. Cure the epoxy at 100°C for 4 hours.

8. Remove the catheters from the oven and inspect them to make sure that the PDMS cylinders did not slip during the cure. If they did, cut off the tips with a razor blade, and repeat the blocking, priming, and gluing steps with new cylinders.

IV. Laser Micromachining - refer to laser instructions for operating procedure

1. Lay the catheters on some double sided tape in the bottom of a 150mm Petri dish. Place the catheters so that the most distal 6mm are hanging off the end of the tape, and align the catheters as closely to perpendicular to the tape as possible. This will simplify the laser machining.
2. Cut a small piece (~1.5 cm) of PI tubing from the proximal end of one of the catheters, and place it on the tape. This will be used to focus the laser.
3. Warm up the laser as per the operating instruction. Transfer the double sided tape with the catheters to the silicon wafer from the stage of the laser, and locate the focusing PI tubing. Focus the laser and replace the focusing mask with the #20.5 aperture. This gives a circular spot of approximately 35µm diameter.
4. I have found that the following parameters work well for machining 049-I tubing:

Energy (mJ)	100-110
# of Pulses	1000
Pulse Rate (pps)	75
Aperture	20.5

5. Test the parameters on the focusing tube to make sure that they are suitable, and move on to the catheters. Locate the distal plug of epoxy that blocks the catheter, and move 100µm proximally from the edge. This serves as your zero reference on each catheter. Machine the first pair of holes through the catheter here. Move 2mm proximally along the catheter and machine the second pair of holes. Repeat this for all catheters.
6. Remove the catheters from the laser, and rotate each catheter 90° using some forceps and return them to the laser stage. Repeat the machining as before, but this time step off 1mm from the zero mark (100µm proximal from epoxy edge) to machine the first pair of holes. Again, move 2mm proximally and machine the final pair of holes. Repeat this for each catheter. Each catheter should now have four pairs of holes spaced 1mm apart, and each successive pair should be rotated by 90° from the last.

V. Finishing and Packaging

1. Place the proximal ends of the catheters into polypropylene injection hubs (27-30G, Smallparts Inc.). Ensure that the proximal tip of the catheter extends to the end of the hub so that it will be easy to suture-load the finished catheters.
2. Glue the catheters in place using Miller Stephenson 907 epoxy (prepared as before). Use a small sliver of plastic or wood to apply the epoxy around the base of the catheter. Use the anti-static gun if it becomes difficult to cleanly apply the epoxy to the hub. Try to fill the reservoir at the base with epoxy to ensure a good seal.
3. Cure the epoxy either overnight, or in the oven at 80°C for 1 hour.

Notes

1. Handling these catheters during the fabrication without damaging them takes practice, but the correct forceps helps immensely. When picking up the PI catheter tubing it is best to use some broad tipped forceps that don't require much closing pressure. This minimizes the chances that the catheters will be crushed or kinked by the handling.
2. For handling the PDMS cylinders it is best to use some extra fine tipped forceps that allow you to pick up the 1mm cylinders cleanly. When carrying out the gluing step, it is best not actually hold the PDMS cylinder. Pick up the cylinder, gently open the forceps and the cylinder will stick to one of the forceps tips. This will make it easier to cleanly attach the cylinder to the catheter tip.

REFERENCES

[1] Yang, M. B., Tamargo, R. J., and Brem, H. *Cancer Res* **49**(18), 5103–5107 Sep (1989).

[2] Tamargo, R. J., Myseros, J. S., Epstein, J. I., Yang, M. B., Chasin, M., and Brem, H. *Cancer Res* **53**(2), 329–333 Jan (1993).

[3] Dang, W., Colvin, O. M., Brem, H., and Saltzman, W. M. *Cancer Res* **54**(7), 1729–1735 Apr (1994).

[4] Walter, K. A., Cahan, M. A., Gur, A., Tyler, B., Hilton, J., Colvin, O. M., Burger, P. C., Domb, A., and Brem, H. *Cancer Res* **54**(8), 2207–2212 Apr (1994).

[5] Tamargo, R. J., Sills, A. K., Reinhard, C. S., Pinn, M. L., Long, D. M., and Brem, H. *J Neurosurg* **74**(6), 956–961 Jun (1991).

[6] Krewson, C. E. and Saltzman, W. M. *Brain Res* **727**(1-2), 169–181 Jul (1996).

[7] Mahoney, M. J. and Saltzman, W. M. *Proc Natl Acad Sci U S A* **96**(8), 4536–4539 Apr (1999).

[8] Tamargo, R. J., Rossell, L. A., Kossoff, E. H., Tyler, B. M., Ewend, M. G., and Aryanpur, J. J. *Epilepsy Res* **48**(3), 145–155 Feb (2002).

[9] Bobo, R. H., Laske, D. W., Akbasak, A., Morrison, P. F., Dedrick, R. L., and Oldfield, E. H. *Proc Natl Acad Sci U S A* **91**(6), 2076–2080 Mar (1994).

[10] Lonser, R. R., Corthésy, M. E., Morrison, P. F., Gogate, N., and Oldfield, E. H. *J Neurosurg* **91**(2), 294–302 Aug (1999).

[11] Groothuis, D. R., Ward, S., Itskovich, A. C., Dobrescu, C., Allen, C. V., Dills, C., and Levy, R. M. *J Neurosurg* **90**(2), 321–331 Feb (1999).

[12] Laske, D. W., Morrison, P. F., Lieberman, D. M., Corthesy, M. E., Reynolds, J. C., Stewart-Henney, P. A., Koong, S. S., Cummins, A., Paik, C. H., and

Oldfield, E. H. *J Neurosurg* **87**(4), 586–594 Oct (1997).

[13] Lieberman, D. M., Laske, D. W., Morrison, P. F., Bankiewicz, K. S., and Oldfield, E. H. *J Neurosurg* **82**(6), 1021–1029 Jun (1995).

[14] Lonser, R. R., Walbridge, S., Garmestani, K., Butman, J. A., Walters, H. A., Vortmeyer, A. O., Morrison, P. F., Brechbiel, M. W., and Oldfield, E. H. *J Neurosurg* **97**(4), 905–913 Oct (2002).

[15] Hamilton, J. F., Morrison, P. F., Chen, M. Y., Harvey-White, J., Pernaute, R. S., Phillips, H., Oldfield, E., and Bankiewicz, K. S. *Exp Neurol* **168**(1), 155–161 Mar (2001).

[16] Yang, W., Barth, R. F., Adams, D. M., Ciesielski, M. J., Fenstermaker, R. A., Shukla, S., Tjarks, W., and Caligiuri, M. A. *Cancer Res* **62**(22), 6552–6558 Nov (2002).

[17] Groothuis, D. R., Benalcazar, H., Allen, C. V., Wise, R. M., Dills, C., Dobrescu, C., Rothholtz, V., and Levy, R. M. *Brain Res* **856**(1-2), 281–290 Feb (2000).

[18] Mardor, Y., Roth, Y., Lidar, Z., Jonas, T., Pfeffer, R., Maier, S. E., Faibel, M., Nass, D., Hadani, M., Orenstein, A., Cohen, J. S., and Ram, Z. *Cancer Res* **61**(13), 4971–4973 Jul (2001).

[19] Lidar, Z., Mardor, Y., Jonas, T., Pfeffer, R., Faibel, M., Nass, D., Hadani, M., and Ram, Z. *J Neurosurg* **100**(3), 472–479 Mar (2004).

[20] Kunwar, S., Prados, M. D., Chang, S. M., Berger, M. S., Lang, F. F., Piepmeier, J. M., Sampson, J. H., Ram, Z., Gutin, P. H., Gibbons, R. D., Aldape, K. D., Croteau, D. J., Sherman, J. W., Puri, R. K., and Group, C. B. I. S. *J Clin Oncol* **25**(7), 837–844 Mar (2007).

[21] Sampson, J. H., Akabani, G., Archer, G. E., Bigner, D. D., Berger, M. S., Friedman, A. H., Friedman, H. S., Herndon, J. E., Kunwar, S., Marcus, S.,

McLendon, R. E., Paolino, A., Penne, K., Provenzale, J., Quinn, J., Reardon, D. A., Rich, J., Stenzel, T., Tourt-Uhlig, S., Wikstrand, C., Wong, T., Williams, R., Yuan, F., Zalutsky, M. R., and Pastan, I. *J Neurooncol* **65**(1), 27–35 Oct (2003).

[22] Weber, F., Asher, A., Bucholz, R., Berger, M., Prados, M., Chang, S., Bruce, J., Hall, W., Rainov, N. G., Westphal, M., Warnick, R. E., Rand, R. W., Floeth, F., Rommel, F., Pan, H., Hingorani, V. N., and Puri, R. K. *J Neurooncol* **64**(1-2), 125–137 (2003).

[23] Worgall, S., Sondhi, D., Hackett, N. R., Kosofsky, B., Kekatpure, M. V., Neyzi, N., Dyke, J. P., Ballon, D., Heier, L., Greenwald, B. M., Christos, P., Mazumdar, M., Souweidane, M. M., Kaplitt, M. G., and Crystal, R. G. *Hum Gene Ther* **19**(5), 463–474 May (2008).

[24] Ren, H., Boulikas, T., Lundstrom, K., Söling, A., Warnke, P. C., and Rainov, N. G. *J Neurooncol* **64**(1-2), 147–154 (2003).

[25] Szarowski, D. H., Andersen, M. D., Retterer, S., Spence, A. J., Isaacson, M., Craighead, H. G., Turner, J. N., and Shain, W. *Brain Res* **983**(1-2), 23–35 Sep (2003).

[26] Morrison, P. F., Chen, M. Y., Chadwick, R. S., Lonser, R. R., and Oldfield, E. H. *Am J Physiol* **277**(4 Pt 2), R1218–R1229 Oct (1999).

[27] Haller, M. F. and Saltzman, W. M. *Pharm Res* **15**(3), 377–385 Mar (1998).

[28] Chen, J., Wise, K. D., Hetke, J. F., and Bledsoe, S. C. *IEEE Trans Biomed Eng* **44**(8), 760–769 Aug (1997).

[29] Rathnasingham, R., Kipke, D. R., Bledsoe, S. C., and McLaren, J. D. *IEEE Trans Biomed Eng* **51**(1), 138–145 Jan (2004).

[30] Neeves, K. B., Lo, C. T., Foley, C. P., Saltzman, W. M., and Olbricht, W. L. *J Control Release* **111**(3), 252–262 Apr (2006).

[31] Turner, J. N., Shain, W., Szarowski, D. H., Andersen, M., Martins, S., Isaacson, M., and Craighead, H. *Exp Neurol* **156**(1), 33–49 Mar (1999).

[32] Guarnieri, M., Carson, B. S., Khan, A., Penno, M., and Jallo, G. I. *J Neurosci Methods* **144**(2), 147–152 Jun (2005).

[33] Gill, S. S., Patel, N. K., Hotton, G. R., O'Sullivan, K., McCarter, R., Bunnage, M., Brooks, D. J., Svendsen, C. N., and Heywood, P. *Nat Med* **9**(5), 589–595 May (2003).

[34] Lang, A. E., Gill, S., Patel, N. K., Lozano, A., Nutt, J. G., Penn, R., Brooks, D. J., Hotton, G., Moro, E., Heywood, P., Brodsky, M. A., Burchiel, K., Kelly, P., Dalvi, A., Scott, B., Stacy, M., Turner, D., Wooten, V. G. F., Elias, W. J., Laws, E. R., Dhawan, V., Stoessl, A. J., Matcham, J., Coffey, R. J., and Traub, M. *Ann Neurol* **59**(3), 459–466 Mar (2006).

[35] Salvatore, M. F., Ai, Y., Fischer, B., Zhang, A. M., Grondin, R. C., Zhang, Z., Gerhardt, G. A., and Gash, D. M. *Exp Neurol* **202**(2), 497–505 Dec (2006).

[36] Holland, E. C. *Proc Natl Acad Sci U S A* **97**(12), 6242–6244 Jun (2000).

[37] Vogelbaum, M. A., Sampson, J. H., Kunwar, S., Chang, S. M., Shaffrey, M., Asher, A. L., Lang, F. F., Croteau, D., Parker, K., Grahn, A. Y., Sherman, J. W., Husain, S. R., and Puri, R. K. *Neurosurgery* **61**(5), 1031–7; discussion 1037–8 Nov (2007).

[38] Saito, R., Krauze, M. T., Noble, C. O., Drummond, D. C., Kirpotin, D. B., Berger, M. S., Park, J. W., and Bankiewicz, K. S. *Neuro Oncol* **8**(3), 205–214 Jul (2006).

[39] Krauze, M. T., Noble, C. O., Kawaguchi, T., Drummond, D., Kirpotin, D. B., Yamashita, Y., Kullberg, E., Forsayeth, J., Park, J. W., and Bankiewicz, K. S. *Neuro Oncol* **9**(4), 393–403 Oct (2007).

[40] Yamashita, Y., Krauze, M. T., Kawaguchi, T., Noble, C. O., Drummond,

D. C., Park, J. W., and Bankiewicz, K. S. *Neuro Oncol* **9**(1), 20–28 Jan (2007).

[41] Chu, C. C. *J Biomed Mater Res* **16**(2), 117–124 Mar (1982).

[42] Athanasiou, K. A., Niederauer, G. G., and Agrawal, C. M. *Biomaterials* **17**(2), 93–102 Jan (1996).

[43] Cohen, S., Yoshioka, T., Lucarelli, M., Hwang, L. H., and Langer, R. *Pharm Res* **8**(6), 713–720 Jun (1991).

[44] Mooney, D. J., Mazzoni, C. L., Breuer, C., McNamara, K., Hern, D., Vacanti, J. P., and Langer, R. *Biomaterials* **17**(2), 115–124 Jan (1996).

[45] Vozzi, G., Flaim, C., Ahluwalia, A., and Bhatia, S. *Biomaterials* **24**(14), 2533–2540 Jun (2003).

[46] King, K., Wang, C., Kaazempur-Mofrad, M., Vacanti, J., and Borenstein, J. *Advanced Materials* **16**(22), 2007–2012 (2004).

[47] Yang, Y., Basu, S., Tomasko, D. L., Lee, L. J., and Yang, S.-T. *Biomaterials* **26**(15), 2585–2594 May (2005).

[48] Grayson, A. C. R., Cima, M. J., and Langer, R. *Biomaterials* **26**(14), 2137–2145 May (2005).

[49] Oh, S., Odland, R., Wilson, S. R., Kroeger, K. M., Liu, C., Lowenstein, P. R., Castro, M. G., Hall, W. A., and Ohlfest, J. R. *J Neurosurg* **107**(3), 568–577 Sep (2007).

[50] Rosen, G. D., Williams, A. G., Capra, J. A., Connolly, M. T., Cruz, B., Lu, L., Airey, D. C., Kulkarni, K., and Williams, R. W. (2000).

[51] Nicholson, C. *Reports On Progress In Physics* **64**(7), 815–884 July (2001).

[52] Sanders, L. M., Kell, B. A., McRae, G. I., and Whitehead, G. W. *J Pharm Sci* **75**(4), 356–360 Apr (1986).

[53] Shain, W., Spataro, L., Dilgen, J., Haverstick, K., Retterer, S., Isaacson, M., Saltzman, M., and Turner, J. N. *IEEE Trans Neural Syst Rehabil Eng* **11**(2),

186–188 Jun (2003).

[54] Spataro, L., Dilgen, J., Retterer, S., Spence, A. J., Isaacson, M., Turner, J. N., and Shain, W. *Exp Neurol* **194**(2), 289–300 Aug (2005).

[55] Takeuchi, S., Ziegler, D., Yoshida, Y., Mabuchi, K., and Suzuki, T. *Lab Chip* **5**(5), 519–523 May (2005).

[56] Gregory, T. F., Rennels, M. L., Blaumanis, O. R., and Fujimoto, K. *J Neurosci Methods* **14**(1), 5–14 Jun (1985).

[57] Ichimura, T., Fraser, P. A., and Cserr, H. F. *Brain Res* **545**(1-2), 103–113 Apr (1991).

[58] Patek, P. *The Anatomical Record* **88**(1), 1–24 (1944).

[59] Rennels, M. L., Gregory, T. F., Blaumanis, O. R., Fujimoto, K., and Grady, P. A. *Brain Res* **326**(1), 47–63 Feb (1985).

[60] Weed, L. *American Journal of Anatomy* **31**(3), 191–221 (1923).

[61] Woollam, D. H. and Millen, J. W. *J Anat* **89**(2), 193–200 Apr (1955).

[62] Cserr, H. F. and Ostrach, L. H. *Exp Neurol* **45**(1), 50–60 Oct (1974).

[63] Cunningham, J., Pivirotto, P., Bringas, J., Suzuki, B., Vijay, S., Sanftner, L., Kitamura, M., Chan, C., and Bankiewicz, K. S. *Mol Ther* **16**(7), 1267–1275 Jul (2008).

[64] Hadaczek, P., Yamashita, Y., Mirek, H., Tamas, L., Bohn, M. C., Noble, C., Park, J. W., and Bankiewicz, K. *Mol Ther* **14**(1), 69–78 Jul (2006).

[65] Krauze, M. T., Saito, R., Noble, C., Bringas, J., Forsayeth, J., McKnight, T. R., Park, J., and Bankiewicz, K. S. *Exp Neurol* **196**(1), 104–111 Nov (2005).

[66] Mamot, C., Nguyen, J. B., Pourdehnad, M., Hadaczek, P., Saito, R., Bringas, J. R., Drummond, D. C., Hong, K., Kirpotin, D. B., McKnight, T., Berger, M. S., Park, J. W., and Bankiewicz, K. S. *J Neurooncol* **68**(1), 1–9 May (2004).

[67] Saito, R., Krauze, M. T., Noble, C. O., Drummond, D. C., Kirpotin, D. B., Berger, M. S., Park, J. W., and Bankiewicz, K. S. *Neuro Oncol* **8**(3), 205–214 Jul (2006).

[68] Denk, W., Strickler, J. H., and Webb, W. W. *Science* **248**, 73–76 (1990).

[69] Squirrell, J. M., Wokosin, D. L., White, J. G., and Bavister, B. D. *Nat Biotechnol* **17**(8), 763–7 (1999).

[70] Denk, W., Delaney, K. R., Kleinfeld, D., Strowbridge, B., Tank, D. W., and Yuste, R. *Journal of Neuroscience Methods* **54**, 151–162 (1994).

[71] Kleinfeld, D., Mitra, P. P., Helmchen, F., and Denk, W. *Proceedings of the National Academy of Sciences USA* **95**, 15741–15746 (1998).

[72] Svoboda, K., Denk, W., Kleinfeld, D., and Tank, D. W. *Nature* **385**, 161–165 (1997).

[73] Neeves, K. B., Sawyer, A. J., Foley, C. P., Saltzman, W. M., and Olbricht, W. L. *Brain Res* **1180**, 121–132 Nov (2007).

[74] Bezemer, J. M., Grijpma, D. W., Dijkstra, P. J., van Blitterswijk, C. A., and Feijen, J. *J Control Release* **62**(3), 393–405 Dec (1999).

[75] Stroh, M., Zipfel, W. R., Williams, R. M., Webb, W. W., and Saltzman, W. M. *Biophys J* **85**(1), 581–588 Jul (2003).

[76] Thorne, R. G. and Nicholson, C. *Proc Natl Acad Sci U S A* **103**(14), 5567–5572 Apr (2006).

[77] Rosamond, W., Flegal, K., Furie, K., Go, A., Greenlund, K., Haase, N., Hailpern, S. M., Ho, M., Howard, V., Kissela, B., Kittner, S., Lloyd-Jones, D., McDermott, M., Meigs, J., Moy, C., Nichol, G., O'Donnell, C., Roger, V., Sorlie, P., Steinberger, J., Thom, T., Wilson, M., Hong, Y., Committee, A. H. A. S., and Subcommittee, S. S. *Circulation* **117**(4), e25–146 Jan (2008).

[78] Barber, P. A., Davis, S. M., Infeld, B., Baird, A. E., Donnan, G. A., Jolley, D.,

and Lichtenstein, M. *Stroke* **29**(12), 2522–2528 Dec (1998).

[79] Molina, C. A., Montaner, J., Abilleira, S., Arenillas, J. F., Ribó, M., Huertas, R., Romero, F., and Alvarez-Sabín, J. *Stroke* **32**(12), 2821–2827 Dec (2001).

[80] Molina, C. A., Montaner, J., Abilleira, S., Ibarra, B., Romero, F., Arenillas, J. F., and Alvarez-Sabín, J. *Stroke* **32**(5), 1079–1084 May (2001).

[81] Fiehler, J., Remmele, C., Kucinski, T., Rosenkranz, M., Thomalla, G., Weiller, C., Zeumer, H., and Röther, J. *Cerebrovasc Dis* **19**(2), 117–124 (2005).

[82] Thomalla, G., Sobesky, J., Köhrmann, M., Fiebach, J. B., Fiehler, J., Weber, O. Z., Kruetzelmann, A., Kucinski, T., Rosenkranz, M., Röther, J., and Schellinger, P. D. *Stroke* **38**(2), 313–318 Feb (2007).

[83] Alexandrov, A. V. and Grotta, J. C. *Neurology* **59**(6), 862–867 Sep (2002).

[84] Kidwell, C. S., Alger, J. R., Salle, F. D., Starkman, S., Villablanca, P., Bentson, J., and Saver, J. L. *Stroke* **30**(6), 1174–1180 Jun (1999).

[85] Kidwell, C. S., Saver, J. L., Mattiello, J., Starkman, S., Vinuela, F., Duckwiler, G., Gobin, Y. P., Jahan, R., Vespa, P., Kalafut, M., and Alger, J. R. *Ann Neurol* **47**(4), 462–469 Apr (2000).

[86] Kidwell, C. S., Saver, J. L., Starkman, S., Duckwiler, G., Jahan, R., Vespa, P., Villablanca, J. P., Liebeskind, D. S., Gobin, Y. P., Vinuela, F., and Alger, J. R. *Ann Neurol* **52**(6), 698–703 Dec (2002).

[87] Baron, J.-C. *Cerebrovasc Dis* **20 Suppl 2**, 25–31 (2005).

[88] Collen, D. *J Cell Biochem* **33**(2), 77–86 Feb (1987).

[89] *N Engl J Med* **333**(24), 1581–1587 Dec (1995).

[90] Katzan, I. L., Furlan, A. J., Lloyd, L. E., Frank, J. I., Harper, D. L., Hinchey, J. A., Hammel, J. P., Qu, A., and Sila, C. A. *JAMA* **283**(9), 1151–1158 Mar (2000).

[91] Gobin, Y. P., Starkman, S., Duckwiler, G. R., Grobelny, T., Kidwell, C. S.,

Jahan, R., Pile-Spellman, J., Segal, A., Vinuela, F., and Saver, J. L. *Stroke* **35**(12), 2848–2854 Dec (2004).

[92] Ly, J. V., Zavala, J. A., and Donnan, G. A. *Expert Opin Pharmacother* **7**(12), 1571–1581 Aug (2006).

[93] Aspey, B. S., Cohen, S., Patel, Y., Terruli, M., and Harrison, M. J. *Neuropathol Appl Neurobiol* **24**(6), 487–497 Dec (1998).

[94] Ma, J., Zhao, L., and Nowak, T. S. *J Neurosci Methods* **156**(1-2), 76–83 Sep (2006).

[95] Spratt, N. J., Fernandez, J., Chen, M., Rewell, S., Cox, S., van Raay, L., Hogan, L., and Howells, D. W. *J Neurosci Methods* **155**(2), 285–290 Sep (2006).

[96] Longa, E. Z., Weinstein, P. R., Carlson, S., and Cummins, R. *Stroke* **20**(1), 84–91 Jan (1989).

[97] Yang, Y., Shuaib, A., and Li, Q. *J Neurosci Methods* **84**(1-2), 9–16 Oct (1998).

[98] Schwarz, A. J., Danckaert, A., Reese, T., Gozzi, A., Paxinos, G., Watson, C., Merlo-Pich, E. V., and Bifone, A. *Neuroimage* **32**(2), 538–550 Aug (2006).

[99] He, Z., Yang, S. H., Naritomi, H., Yamawaki, T., Liu, Q., King, M. A., Day, A. L., and Simpkins, J. W. *J Neurol Sci* **182**(1), 16–28 Dec (2000).

[100] Cheung, K. C., Renaud, P., Tanila, H., and Djupsund, K. *Biosensors and Bioelectronics* **22**(8), 1783–1790 March (2007).

[101] Mercanzini, A., Cheung, K., Buhl, D. L., Boers, M., Maillard, A., Colin, P., Bensadoun, J.-C., Bertsch, A., and Renaud, P. *Sensors and Actuators A: Physical* **143**(1), 90–96 May (2008).

[102] Yeager, J. D., Phillips, D. J., Rector, D. M., and Bahr, D. F. *Journal of Neuroscience Methods* **173**(2), 279–285 August (2008).